

# JGR Biogeosciences

## RESEARCH ARTICLE

10.1029/2022JG006924

### Key Points:

- An integrated modeling system was constructed for the Pearl River Estuary to diagnose the phytoplankton response after Typhoon Hato
- The increased discharge after Hato halved the residence time and doubled the decay rate of the water mass within Lingding Bay
- The uplifted nutrient-rich subsurface water and the riverine nutrient export jointly support the offshore phytoplankton bloom

### Supporting Information:

Supporting Information may be found in the online version of this article.

### Correspondence to:

Y. Feng,  
[yfeng1982@126.com](mailto:yfeng1982@126.com)

### Citation:

Feng, Y., Huang, J., Du, Y., Balaguru, K., Ma, W., Feng, Q., et al. (2022). Drivers of phytoplankton variability in and near the Pearl River Estuary, South China Sea during Typhoon Hato (2017): A numerical study. *Journal of Geophysical Research: Biogeosciences*, 127, e2022JG006924. <https://doi.org/10.1029/2022JG006924>








Received 5 APR 2022

Accepted 24 SEP 2022

### Author Contributions:

**Conceptualization:** Yang Feng, Yan Du, Karthik Balaguru  
**Data curation:** Xianghui Guo, Shuqun Cai  
**Formal analysis:** Jingwen Huang, Youchang Zheng, Xianghui Guo  
**Funding acquisition:** Shuqun Cai  
**Methodology:** Yang Feng, Jingwen Huang, Weiwei Ma, Qingyu Feng, Xiuquan Wan  
**Supervision:** Yang Feng  
**Writing – original draft:** Yang Feng  
**Writing – review & editing:** Yan Du, Karthik Balaguru, Xianghui Guo

## Drivers of Phytoplankton Variability in and Near the Pearl River Estuary, South China Sea During Typhoon Hato (2017): A Numerical Study

Yang Feng<sup>1,2</sup> , Jingwen Huang<sup>2,3</sup>, Yan Du<sup>1,2</sup> , Karthik Balaguru<sup>4</sup> , Weiwei Ma<sup>5</sup> , Qingyu Feng<sup>6</sup>, Xiuquan Wan<sup>5</sup> , Youchang Zheng<sup>3</sup>, Xianghui Guo<sup>7</sup> , and Shuqun Cai<sup>1,2</sup> 

<sup>1</sup>Southern Marine Science and Engineering Guangdong Laboratory (Guangzhou), Guangzhou, China, <sup>2</sup>State Key Laboratory of Tropical Oceanography, South China Sea Institute of Oceanology & Innovation Academy of South China Sea Ecology and Environmental Engineering, Chinese Academy of Sciences, Guangzhou, China, <sup>3</sup>University of Chinese Academy of Sciences, Beijing, China, <sup>4</sup>Pacific Northwest National Laboratory, Richland, WA, USA, <sup>5</sup>College of Oceanic and Atmospheric Sciences, Ocean University of China, Qingdao, China, <sup>6</sup>State Key Laboratory of Urban and Regional Ecology, Research Center for Eco-Environmental Sciences, Chinese Academy of Sciences, Beijing, China, <sup>7</sup>State Key Laboratory of Marine Environmental Science, College of Ocean and Earth Sciences, Xiamen University, Xiamen, China

**Abstract** The Pearl River Estuary and adjacent seas in South China Sea are frequently affected by tropical cyclones (TCs). Previous in situ and remote sensing studies have found that typhoons can enhance phytoplankton biomass and induce blooms in this region. However, the mechanistic links between phytoplankton blooms and typhoons have not been well understood due to the interplay of multiple complex processes along the land-ocean-atmosphere interface. Here, we constructed an integrated modeling system with the marine ecosystem and sediment components for the China Great Bay Area. By using the integrated modeling system, we quantitatively investigated the phytoplankton response to hydrological conditions variations under Typhoon Hato (2017), a strong typhoon case. Passive tracer experiments showed that with high river discharge induced by heavy rainfall, the residence time within Lingding Bay is as short as 15 days, less than half of that under the climatological discharge. The increase in freshwater pulse washes out the phytoplankton biomass within Lingding Bay. While for the offshore region, the analysis of various source and sink terms for the offshore region's post-typhoon response showed that the increase of phytoplankton biomass in the first week was because of the uplift of nutrient-rich subsurface water, while in the second week, it was due to the seaward propagation of nearshore high phytoplankton biomass water. While riverine nutrients support phytoplankton growth in the third week, a large part of phytoplankton biomass was lost to zooplankton grazing, showing the system shifted from the bottom-up control to the top-down control.

**Plain Language Summary** Several previous satellite-based studies observed phytoplankton blooms within the Pearl River estuary-coastal system after the passage of Typhoons. However, the mechanisms controlling the occurrence of the bloom are not very well known. Here, we introduce a comprehensive modeling system to quantitatively diagnose the relative importance of multiple processes in regulating the phytoplankton bloom from the inner bay to the outer shelf. By taking a strong typhoon case, Hato (2017), as an example, we found that much of the phytoplankton was washed out of the Lingding Bay after Hato. The nearshore phytoplankton bloom occurred 2 weeks after Hato's arrival due to the increased terrestrial runoff after heavy rainfall. For the offshore region, storm-induced upwelling also played a role in increasing the phytoplankton biomass, in addition to the impact from the river discharge. However, the offshore bloom did not occur due to the high grazing impact from the zooplankton.

## 1. Introduction

The Pearl River is the second largest river in China in terms of freshwater discharge, fed by three main tributaries (the West River, the North River, and the East River) and many local rivers. The Pearl River Estuary (PRE) includes three subestuaries, Lingding Bay, Modaomen, and Huangmaohai. About 50%–55% of the freshwater from the Pearl River discharges into the Lingding Bay, which is the focus area of this study. The PRE is located in the central area of the Guangdong-Hong Kong-Macao Greater Bay Area of China. In recent years, with a rapidly growing population and socioeconomic development, input of nutrients and diverse contaminants increased rapidly, which led to a wide range of environmental problems, such as eutrophication, hypoxia,

and ocean acidification (Guo et al., 2020; Hu et al., 2021; Ke et al., 2022; Y. Zhao et al., 2021). Furthermore, during the past decade, the activity of typhoons (also referred to as tropical cyclones [TCs] or hurricanes) has increased because of global warming (Balaguru et al., 2012, 2016; Da et al., 2021; Elsner et al., 2008; Goldenberg et al., 2001; Mei et al., 2015; Webster et al., 2005; Wu et al., 2005). During 1949–2020, there were about 1,942 typhoons in the Northwest Pacific Ocean and the South China Sea (SCS), and about 3 of them hit the coast of the northern SCS per year during the summer monsoon season on average (G. Pan et al., 2017; Wang et al., 2007).

Typhoons play an important role in phytoplankton blooms and primary productivity for the PRE and adjacent seas (H. Liu et al., 2013; S. Liu et al., 2020; J. Pan et al., 2018). By using satellite remote sensing data with field observations, previous research found that typhoons can trigger phytoplankton blooms in and near the PRE, as well as the offshore regions of the SCS (D. Qiu et al., 2019; Ye et al., 2013; H. Zhao et al., 2009, 2017; Zheng & Tang, 2007). The processes that were proposed to play a role in the blooms include wind-induced vertical mixing, terrestrial precipitation, freshwater discharge, nutrient input, the after-typhoon wind-driven circulation, and strong near-inertial oscillations. Although these in situ and satellite-based studies provide insights into the response of phytoplankton variability to hydrodynamic conditions under extreme weather conditions, they were limited in evaluating the relative importance of physical and biological processes. For example, the high surface chlorophyll-*a* (Chl-*a*) concentration observed in the coastal region can be caused by various processes, such as the horizontal advection of phytoplankton from the estuary, upward entrainment of phytoplankton from the subsurface Chl-*a* maximum and new production of Chl-*a* due to enhanced nutrient concentration by horizontal advection and vertical mixing, whose relative significance is less clear. In addition, typhoons are usually associated with intense rainfall and cloud cover, substantially reducing satellite data availability (Chang et al., 2008). Besides, the subsurface Chl-*a* bloom, which may be stronger and longer in duration than the surface signal, may not be well captured by remote sensing methods (Chai et al., 2021; Ye et al., 2013).

Numerical models are invaluable tools for untangling the relative roles of physical and biological processes under extreme weather conditions and assessing the influence of subsurface processes. Fujii and Yamanaka (2008) developed ecosystem models for the subarctic western North Pacific to investigate the response of primary production to storms. However, their models are embedded in idealized physical frameworks, suggesting that studies using numerical models with more realistic physics are needed. G. Pan et al. (2017) used a coupled physical-biogeochemical model to study the phytoplankton response to all typhoons that affected the SCS during 2000–2009. They found over 50% of typhoons triggered phytoplankton blooms, and 44% of those blooms happened in the coastal ocean. Although their model includes the general features of ocean dynamics (mixing, entrainment, and upwelling), the effects of an increased river discharge after rainfall, which is well-known to contribute to the coastal bloom significantly, were not considered. As a matter of fact, the phytoplankton response of the shallow ocean in coastal regions is very complicated, involving land, ocean, atmosphere, biogeochemical, and sediment processes. For example, typhoon-induced upwelling and vertical mixing can overcome the upper-ocean stratification, and entrain nutrients from the subsurface into the euphotic layer, which can support phytoplankton growth and increase the primary production (Y. Liu et al., 2019). Additionally, the storm-induced resuspended sediments can influence water transparency and remineralization, which may also impact phytoplankton blooms ultimately (Bianucci et al., 2018; N. Chen et al., 2018).

In summary, we need an integrated modeling system to better simulate the ecological environment under extreme weather conditions. Here, we investigate phytoplankton dynamics from an ecosystem model that is coupled to a Land-Ocean-Atmosphere modeling system for the PRE. Taking Typhoon Hato as an example, we analyzed environmental differences and, phytoplankton source and sink terms along the ecological gradient from high-nutrient plume waters to low-nutrient offshore waters, focusing on the quantification of phytoplankton variability to a change in hydrological conditions. Hato was a strong typhoon that formed in the western Pacific and rapidly intensified into a Category 3 intense typhoon (increased 10 kt within 3 hr) just before making landfall near Zhuhai City, Guangdong Province, on August 23, 2017. According to the Statistics and Census Service of Macau, Hato severely devastated the city, with 10 fatalities and estimated economic losses exceeding US\$1.5 billion (<http://www.nmdis.org.cn/hygb/zghyzhgb/>).

The study is organized as follows. Section 2 presents the configuration of the integrated land-ocean-atmosphere modeling system with marine ecosystem and sediment resuspension components. In Section 3, we present model validation with satellite observations and biophysical conditions for the PRE-coastal system during, pre-, and

post-Hato. Section 4 provides a discussion on predominant processes affecting phytoplankton biomass within the mixed layer depth (MLD), summarizes the findings, and proposes future research.

## 2. Data and Methods

### 2.1. Track of Typhoon Hato

The 6-hr best-track TC data were obtained from the Shanghai Typhoon Institute, China Meteorological Administration (CMA), which includes the location (in longitude and latitude) of the TC center, maximum sustained 10-m height wind speed, and the radius of maximum winds (Figure 1a). The track information reveals that Typhoon Hato formed over the western North Pacific at 128°E, 20.4°N on August 21, 2017. It moved westward and passed the Luzon Strait at about 0000 UTC on August 22 and intensified into a Category 1 typhoon by 0800 UTC on August 22, with the maximum sustained near-surface wind speed increasing to 33 m s<sup>-1</sup>. At 0000 UTC on August 23, Hato was upgraded to a Category 2 typhoon with the maximum sustained near-surface wind speed of 42 m s<sup>-1</sup>. About 3 hr later, Hato reached its peak intensity with a maximum sustained near-surface wind speed of 48 m s<sup>-1</sup>. Finally, Hato made landfall near Zhuhai City (113.2°E, 22.1°N), Guangdong Province, at 0450 UTC on August 23. Soon after its landfall, Hato weakened rapidly to 30 m s<sup>-1</sup> in several hours and dissipated by 0800 UTC on August 24.

### 2.2. Satellite Observations

In situ measurements of physical and biological environments under extreme weather conditions are rare. In this study, we used weekly composites from GlobColour (<https://hermes.acri.fr/>), which provide a continuous data set of merged L3 Ocean Color products for surface chlorophyll distribution before (August 15–21), during (August 22–28), 1 week (August 29 to September 4), and 2 weeks (September 5–11) after Hato's landfall to validate our biogeochemical model. We also used maps of ocean salinity from National Aeronautics and Space Administration (NASA) Soil Moisture Active Passive (SMAP) missions [https://data.remss.com/smap/SSS/V04.0/FINAL/L3/8day\\_running/](https://data.remss.com/smap/SSS/V04.0/FINAL/L3/8day_running/) to validate our simulated sea surface salinity. Despite SMAP SSS having been documented to exhibit bias compared to Argo SSS in shallow waters near river mouths, the variability was widely used to determine the plume patterns (Fournier & Lee, 2021).

### 2.3. The Guangdong-Hong Kong-Marco Great Bay Area Modeling System

#### 2.3.1. The Modeling System Compartments

Our modeling system covers the northern part of the SCS (Figure 1). The ocean-atmosphere components are based on the Coupled Ocean-Atmosphere-Wave-Sediment Transport (COAWST) modeling system, which consists of the Weather Research Forecasting (WRF) model and the Regional Ocean Modeling System (ROMS) (Warner et al., 2008, 2010). The WRF domain spans from 97.70°E to 122.30°E and from 16.25°N to 30.37°N with an averaged horizontal resolution of about 12 km, which covers the entire Pearl River Watershed and northern part of the SCS. The ROMS domain spans the region from 104.98°E to 120.55°E and from 16.54°N to 25.96°N, with an average spatial resolution of about 4 km. The model has 30 terrain-following vertical layers. The physical model is configured to use the recursive MPDATA 3-D advection scheme for tracers, fourth-order horizontal advection of tracers, third-order upwind advection of momentum, and the Mellor and Yamada (1982) turbulence closure scheme for vertical mixing. The Community Sediment Transport Modeling System (CSTMS) was also included to simulate total resuspended sediment concentration during Hato. Three types of sediment (clay, silt, and fine) were defined with different grain diameters and settling velocities. The simulated resuspended sediment concentrations within Lingding Bay, for both nearshore and offshore, are shown in Figure S1 in Supporting Information S1. For more details regarding the sediment model setup and validation, please see Y. Chen et al. (2019). We only considered the hydrodynamic impact on sediment transport, not vice versa, since the sediment concentrations in this region are not high enough to generate turbidity flow and influence the hydrodynamics. The ecosystem model is the Fennel module (Fennel et al., 2006, 2011) that has been embedded in ROMS, which represents a simplified nitrogen cycle with seven state variables: nitrate (NO<sub>3</sub>), ammonium (NH<sub>4</sub>), phytoplankton (Phy), zooplankton (Zoo), small and large detritus (SDet and LDet), and chlorophyll (Chl). Daily river discharge is generated from the land surface model SWAT (Soil and Water Assessment Tool). The model was

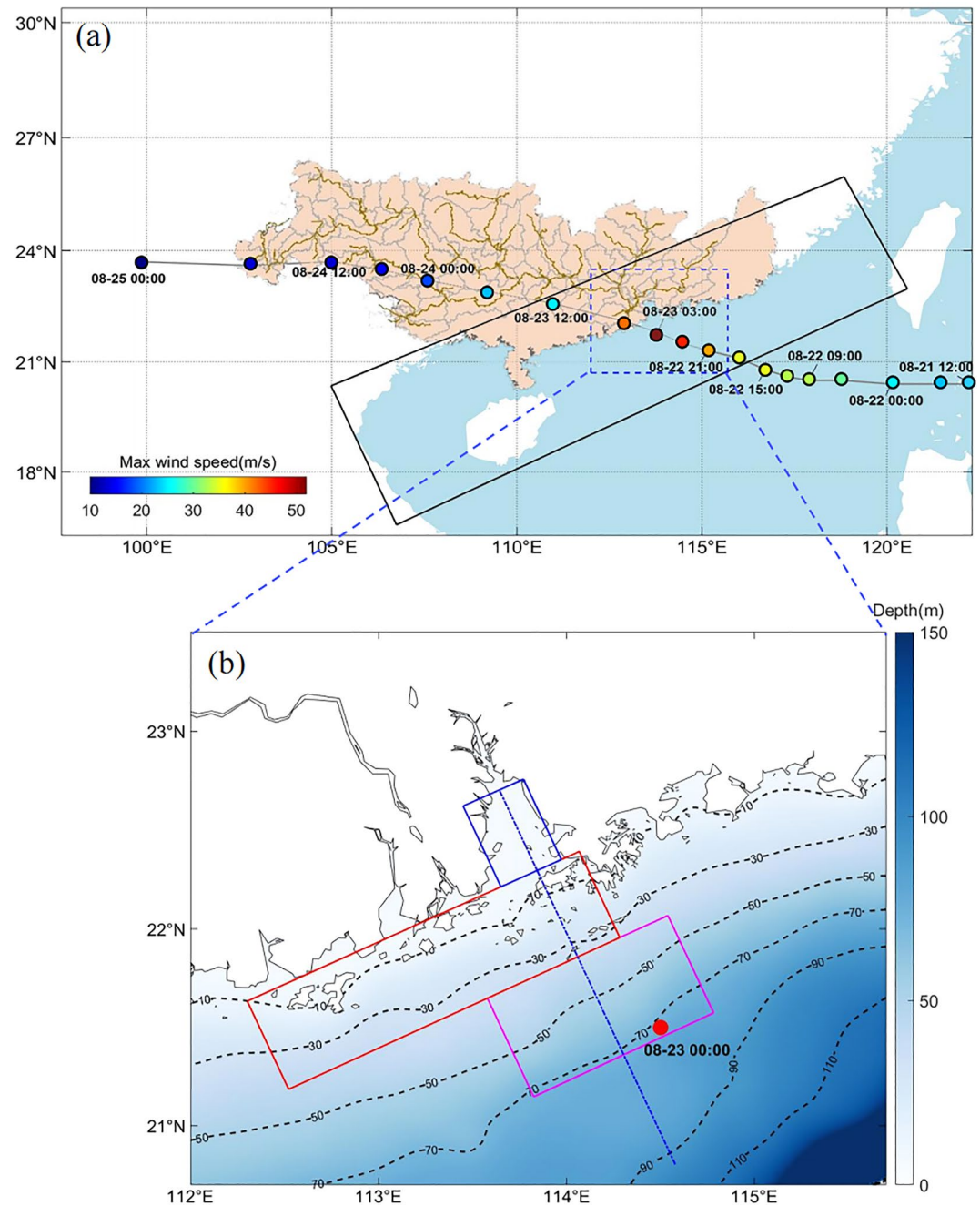


**Figure 1.** Model domains applied in this study. The entire panel (a) is the Weather Research Forecasting (WRF) model domain (12 km resolution). The black box represents the ROMS model domain ( $\sim 4$  km resolution). The blue box with a dashed line ( $20.7\text{--}23.5^{\circ}\text{N}$ ,  $112\text{--}115.7^{\circ}\text{E}$ ) covers the Pearl River estuary (PRE)-coastal systems. More details on the PRE-coastal system are shown in (b). The blue, red, and magenta boxes are Lingding Bay, nearshore (0–30 m), and offshore (30–70 m) regions in Figures 5, 10, and 11. The dashed blue line highlighted the cross-section we focused on analyzing in the main text. Location of Hato on August 23 00:00 was noted, which was the timing of the vertical dashed line in Figure 5.

configured specifically for the Pearl River Basin and has been validated with observed monthly river discharge for the period 2013–2017 from the SCS Sub-Bureau (Figure S2 in Supporting Information S1). WRF atmospheric output at 6-hr intervals, including rain, temperature, wind velocity, relative humidity, and shortwave and longwave radiations, have been used to force the land surface model to generate daily river discharge, especially the extreme levels of discharge caused by the storm. River nutrient concentrations were retrieved from water

samples collected monthly from the eight river outlets of the Pearl River Delta (Lu et al., 2009), including  $\text{NO}_3$ ,  $\text{NH}_4$ , and organic nitrogen. All riverine organic matter was treated as  $\text{SDet}$  in our simulation. The phytoplankton, zooplankton, and  $\text{LDet}$  are all set to zero. The method to treat riverine materials is consistent with other biogeochemical modeling studies in river-dominated estuarine-coastal systems (Feng et al., 2015; Yu et al., 2015). In all model simulations, the river nutrient concentration is kept constant while the loading varies with the changing river discharge. Since the total nitrogen loading is the nutrient concentration multiplied by the river discharge, the loading increases due to typhoon-induced flooding incorporated in this simulation scheme. Since the ecosystem module is the central component for the study, we next describe it in detail.

### 2.3.2. The Ecosystem Module for Phytoplankton Dynamics

The time rate of change of phytoplankton due to biological sources and sinks is given by

$$\frac{\partial \text{Phy}}{\partial t} = \mu \text{Phy} - g \text{Zoo} - m_P \text{Phy} - \tau (\text{SDet} + \text{Phy}) \text{Phy} - w_P \frac{\partial \text{Phy}}{\partial z} \quad (1)$$

where  $\mu$  is the phytoplankton growth rate, which depends on the temperature ( $T$ ) during the period when the growth rate is a maximum ( $\mu_{max} = \mu_{max}(T) = \mu_0 1.066^T$ ) (Eppley, 1972), on the photo-synthetically available radiation  $I$ , and on the nutrient concentration  $\text{NO}_3$  and  $\text{NH}_4$ .

$$\mu = \mu_{max} f(I) (L_{\text{NO}_3} + L_{\text{NH}_4}) \quad (2)$$

where

$$L_{\text{NO}_3} = \frac{\text{NO}_3}{k_{\text{NO}_3} + \text{NO}_3} \frac{1}{1 + \text{NH}_4/k_{\text{NH}_4}} \quad (3)$$

$$L_{\text{NH}_4} = \frac{\text{NH}_4}{k_{\text{NH}_4} + \text{NH}_4} \quad (4)$$

The light available for photosynthesis  $I$  is estimated using the following equation:

$$I = I(z) = I_0 \text{par} \cdot \exp \left( -Z K_w - K_{chl} \int_z^0 \text{Chl}(\vartheta) d\vartheta - K_{sed} \int_z^0 \text{SSC}(\vartheta) d\vartheta \right) \quad (5)$$

where  $I_0$  is the incoming light intensity right below the surface layer,  $Z$  is the water depth, and  $\text{par}$  is the fraction of light that is available for photosynthesis.  $K_w$  and  $K_{chl}$  are the light attenuation coefficients for water and chlorophyll, respectively.  $\text{Chl}(\vartheta)$  represents the concentration of chlorophyll, the dynamics of which were derived from a phytoplankton equation by multiplying the ratio of chlorophyll to phytoplankton biomass.

$$\frac{\partial \text{Chl}}{\partial t} = \rho_{chl} \text{Chl} - g \text{Zoo} \frac{\text{Chl}}{\text{Phy}} - m_P \text{Chl} - \tau (\text{SDet} + \text{Phy}) \text{Chl} \quad (6)$$

where  $\rho_{chl} = \theta_{max} \mu \text{Phy} / \alpha \text{Chl}$ ,  $\theta_{max}$ , and is the maximum ratio of chlorophyll to phytoplankton biomass. We added a new sediment-induced light attenuation term within the original ecosystem model in this equation.  $K_{sed}$  is the light attenuation coefficient due to suspended sediments, and  $\text{SSC}(\vartheta)$  is total suspended sediment concentration in the respective layer.  $\text{SSC}$  was generated from a separate run with the Simulating Waves Nearshore (SWAN) module, CSTMS, and ROMS hydrodynamic module (See below and Figure 2). The function  $f(I)$  represents the photosynthesis-irradiation relationship (Evans & Parslow, 1985)

$$f(I) = \frac{\alpha I}{\sqrt{\mu_{max}^2 + \alpha^2 I^2}} \quad (7)$$

where  $\alpha$  is the initial slope. The phytoplankton loss due to microzooplankton grazing is  $g \text{Zoo}$ , where the grazing rate  $g$  is represented by



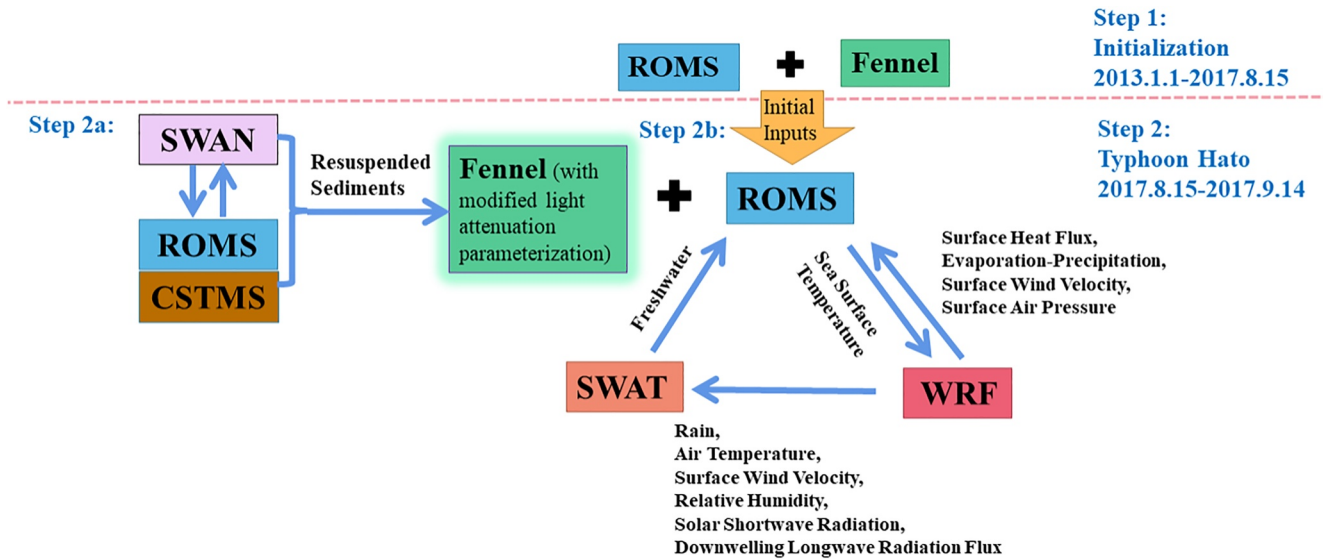


**Figure 2.** Flow chart of initial (5 years 139 days) and Typhoon Hato simulation (1 month). In step 1, only the coupled hydrodynamic-ecosystem model (ROMS-Fennel) was run, which provides initial inputs for the next period. In step 2a, coupled ocean (ROMS hydrodynamics), sediment transport (CSTMS sediment), and wave module (SWAN) were run to obtain resuspended sediment. In step 2b, coupled atmosphere (WRF atmosphere), land surface model (SWAT land), and modified biogeochemical (Fennel biogeochemistry) modules were run by using the resuspended sediment as an input to estimate light attenuation availability for photosynthesis.

$$g = g_{max} \frac{Phy^2}{k_P + Phy^2} \quad (8)$$

With  $g_{max}$  as the maximum grazing rate and  $k_P$  as the half-saturation concentration for phytoplankton ingestion. Other phytoplankton loss terms are mortality, represented by  $m_P Phy$ , aggregation of phytoplankton and small detritus to large detritus  $\tau(SDet + Phy)Phy$ , where  $\tau$  is the aggregation parameter. Values for the biological model parameters are provided in Table 1.

### 2.3.3. Initial and Boundary Conditions

To obtain a stable initial condition for the biogeochemical variables, we first conducted a 5-year run (from January 1, 2013 to August 15, 2017) using the coupled physical-biogeochemical model with observed river discharge and nutrients. The hydrodynamic and biogeochemical model setup is identical for the spin-up period and the typhoon run. For the atmospheric forcing in the spin-up run, we used the following parameters from ERA-5 reanalysis: longwave radiation, air-pressure, air-humidity, rain, shortwave radiation, air-temperature, and U, V wind fields. Note that the spin-up run is one-way coupled with the ocean being forced by reanalysis atmospheric fields. Since this study focuses on the ocean's biogeochemical response to typhoons, we extracted output from the last day of the spin-up simulation on August 15, 2017, used it as the initial condition and then ran the modeling system for 1 month (August 15 to September 14, 2017) for the Hato simulation (Step 2 of Figure 2). At the open boundary, the physical module is forced by daily averaged temperature, salinity, current velocity, and de-tidal water-level from a high-resolution regional SCS model (Peng et al., 2015). The biogeochemical variables use climatological values based on a historical run of CESM2-WACCM-FV2 (covering the period 2005–2014), a part of CMIP6 (<https://esgf-node.llnl.gov/search/cmip6/>).

### 2.3.4. The Simulation Procedure

To investigate the phytoplankton response to Typhoon Hato, we run the integrated modeling system in three steps: (a) conduct a simulation by coupling the sediment module CSTMS, SWAN, and ROMS hydrodynamic module to obtain a 3D field of resuspended sediments during the typhoon; (b) modify the ecosystem module (the Fennel module) of ROMS to include light attenuation induced by resuspended sediments; (c) the coupled model (ROMS hydrodynamic and ecosystem modules, WRF and SWAT) was run by using the 3D field of resuspended sediment as an input.

**Table 1**  
Definitions of Biogeochemical Parameters Used in State Variable Equations

Symbol	Description	Value	Units
$K_{chl}$	Light attenuation coefficients for chlorophyll	0.02486	$(\text{mgChl m}^{-2})^{-1}$
$K_{NH_4}$	Half-saturation constant for ammonium uptake	0.5	$\text{mmole Nm}^{-3}$
$K_{NO_3}$	Half-saturation constant for nitrate uptake	0.5	$\text{mmole Nm}^{-3}$
$K_P$	Half-saturation concentration of phytoplankton ingestion	2	$(\text{mmole Nm}^{-3})^2$
$K_W$	Light attenuation coefficients for water	0.04	$\text{m}^{-1}$
$K_{sed}$	Light attenuation for sediment	0.052	$\text{m}^{-1}$
$\alpha$	Initial slope of the P-I curve	0.025	$(\text{W m}^{-2})^{-1} \text{day}^{-1}$
$m_P$	Phytoplankton mortality rate	0.15	$\text{day}^{-1}$
$par$	Fraction of light that is available for photosynthesis	0.43	Dimensionless
$g_{max}$	Zooplankton maximum growth rate at 0°C	0.6	$\text{day}^{-1}$
$\mu_0$	Phytoplankton growth rate	0.48	$\text{day}^{-1}$
$\omega_P$	Vertical sinking velocity for phytoplankton	0.1	$\text{day}^{-1}$
$\omega_{LD}$	Vertical sinking velocity for large detritus	5	$\text{day}^{-1}$
$\omega_{SD}$	Vertical sinking velocity for small detritus	0.1	$\text{day}^{-1}$
$\omega_{RS-N}$	Small detritus remineralization rate	0.3	$\text{day}^{-1}$
$\omega_{RL-N}$	Large detritus remineralization rate	0.01	$\text{day}^{-1}$
$\tau$	Aggregation parameter	0.02	$\text{day}^{-1}$

To better describe spatio-temporal variations of the biophysical response during our simulation period, we separated the PRE-coastal system into three regions, Lingding Bay, nearshore (0–30 m), and offshore (30–70 m) (Figure 1b).

#### 2.4. Passive Tracer Experiments and Estimation of Residence Time

The residence time is defined as the time taken by a conservative tracer to leave a control volume. Passive tracers are widely used in numerical models for residence time calculation (Geyer et al., 2000; Monsen et al., 2002; W. G. Zhang et al., 2010; Z. Zhang et al., 2019). To examine how quickly the water mass moves out of Lingding Bay due to the increased runoff by heavy rainfall, we added a conservative passive tracer with concentrations of  $1.0 \text{ kg/m}^3$  in the control volume of Lingding Bay. The tracers were added on August 15, 2017 and we ran the model for the entire Typhoon Hato period. To highlight the influence of river discharge, two additional experiments were also run by switching the SWAT simulated daily river flow with SWAT simulated climatological flow from August 15 to September 14, 2017.

The passive tracers escape the control volume gradually following the movement of the water mass. Thus, the total tracer mass remaining in the control volume  $V$  at the time is the integration of the tracer concentration over the entire control volume.

$$M(t) = \int_V C(t, x) dV \quad (9)$$

The water mass in the control volume is assumed to have been replaced when the tracer mass remaining in the volume falls below 10% of the initial value. Besides, we also calculated the rate of tracer decay ( $\lambda$ ) as:

$$M_t = M_0 e^{-\lambda T} \quad (10)$$

Here  $T$  is the time duration over which the concentration of particles becomes half of its original value.

## 2.5. The Mass Budget Analysis

The surface phytoplankton biomass is regulated by both the physical and biological processes. We integrate the volume of each term in Equation 1 within the surface layer to estimate their relative contribution as follows:

$$\begin{aligned}
 \frac{\partial M_{phy}}{\partial t} = & \underbrace{\iiint_s \left( -v \frac{\partial P_{hy}}{\partial y} \right) dx dy dz}_{\text{cross-shore advection}} + \underbrace{\iiint \left( -u \frac{\partial P_{hy}}{\partial x} \right) dx dy dz}_{\text{along-shore advection}} + \\
 & \underbrace{\iiint \left( -w \frac{\partial P_{hy}}{\partial y} \right) dx dy dz}_{\text{vertical advection}} + \underbrace{\iiint \left( K_v \frac{\partial O_2}{\partial z} \right) dx dy dz}_{\text{vertical diffusion}} + \\
 & \iiint (PP) dx dy dz + \iiint (-G) dx dy dz + \iiint (-M) dx dy dz + \\
 & \iiint (-AGG) dx dy + \iiint (-Sink) dx dy dz
 \end{aligned} \tag{11}$$

where  $M_{phy}$  is the total phytoplankton content (in units of kg-N) within the surface layer. The first term on the right-hand side of the equation is the cross-shore influx of phytoplankton into the offshore region. Similarly, the second term is the along-shore influx of phytoplankton. The third term is the vertical advective flux across the lower boundary, which reflects the contribution of upwelling. The fourth term represents the vertical diffusive flux. In addition to hydrological processes, the fifth to ninth terms represent the phytoplankton produced by primary production (PP), loss to grazing (G), mortality (M), aggregation (AGG), and sinking (Sink), respectively.

## 3. Results

### 3.1. Model Validation

Firstly, we compared the simulated sea surface salinity with SMAP observations (Figure 3). The SMAP Level 3 SSS has a coarse resolution with no data next to the Lingding Bay and nearshore within 20 m isobath. However, the simulated offshore SSS spatio-temporal variability is consistent with that from SMAP before, during, and post-Hato, although the model had higher SSS than SMAP in terms of magnitude. Before Hato, there was relatively low SSS in the offshore region in both satellite data ( $\sim 32.3$  PSU) and simulations ( $\sim 32.9$  PSU) (Figures 3a and 3e and Figure S5e in Supporting Information S1). The salinity increased to higher than 33 PSU during Hato and decreased to  $\sim 31$  PSU 2 weeks later (Figures 3b–3d and 3f–3h and Figure S5e in Supporting Information S1). Within the Lingding Bay and the nearshore region (for areas within the 10 m isobath), SSS was below 26 PSU. Further, the freshwater ( $< 26$  PSU) extended offshore over the 30 m isobath 1 week after Hato (Figures 3c and 3g). We also calculated the deviation of SSS from the mean SSS before, during, and after Hato (Figures 3i–3p). Both the satellite observations and model simulations consistently show positive values between 30 and 70 m 2 weeks after Hato, which is due to the offshore region becoming fresher (Figures 3i and 3p).

Besides, we also compared the simulated salinity field in the spin-up period with cruise data available from June 2017 (Figures S6b and S6d in Supporting Information S1). The results show that the model simulated salinity fields are highly consistent with observations. Quantitative comparison for surface salinity shows that the simulated SSS is lower than the observation by about 0.02 PSU on average. The root mean square difference (RMSD) is 4.23 PSU and the spatial correlation is high ( $\sim 0.93$ ). Considering the subsurface, the simulated salinity is lower than the observed by 2.23 PSU on average. The RMSD is 7.02 PSU and the correlation coefficient is as high as 0.89.

Next, we compared the simulated sea surface chlorophyll concentration with both satellite and in situ-based observations (Figure 4 and Figure S7a in Supporting Information S1). The surface chlorophyll concentration from the model was extremely low in Lingding Bay before Hato (Figure 4e). This is because the river outlets in the model were distributed in the upper part of the Bay and consequently the high freshwater discharge dilutes the surface chlorophyll concentration. While synchronized comparison with cruise-based observations shows that the model



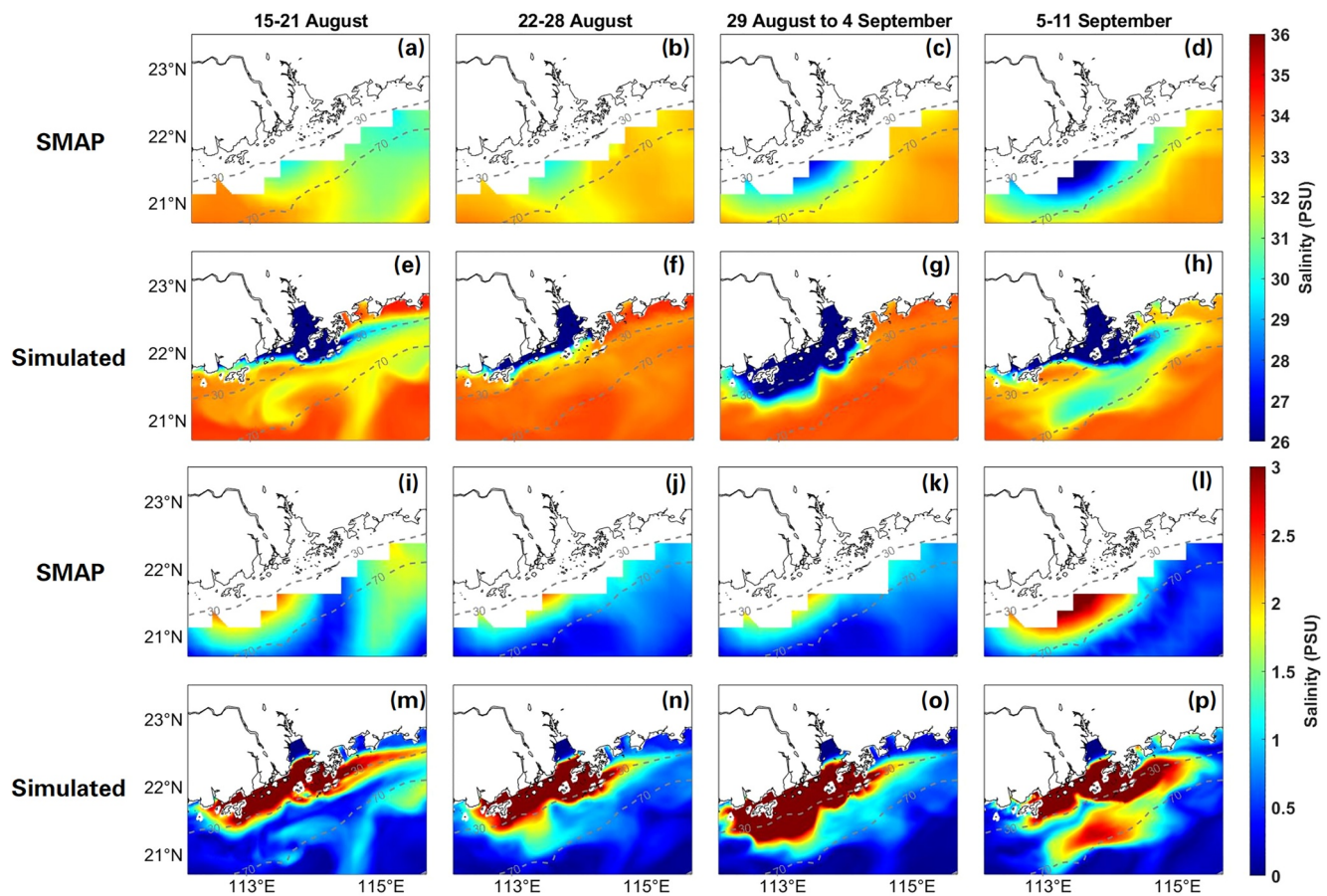


**Figure 3.** Composite of surface salinity (a–h) and deviation (i–p) before (August 15–21) (a, e, i, and m), during (August 22–28) (b, f, j, and n), 1 week after (August 29 to September 4) (c, g, k, and o), and 2 weeks after (September 5–11) (d, h, l, and p) Typhoon Hato. The bathymetry for nearshore (30 m) and offshore separation (70 m) were added as gray dashed lines. The deviation was calculated as the  $\sqrt{\left(D_i - \bar{D}\right)^2}$ , where  $D_i$  is data at the selected period ( $i = 1, 2, 3,$  and  $4$ ),  $\bar{D}$  is the mean of four period overall.

simulated surface chlorophyll is in good agreement with the observed high chlorophyll concentration in the middle and lower part of Lingding Bay despite a slight overestimation (Figure S7a in Supporting Information S1).

In the nearshore region, the satellite observed surface chlorophyll concentration was high within the 30 m isobath before and 1 week after Hato (Figures 4a and 4c). In both simulation and satellite observations, the nearshore surface chlorophyll concentration reduced greatly during Hato's passage (Figures 4b and 4f).

Also, in both satellite observations and model simulation, the high surface chlorophyll concentration extended over the 30-m isobath near the western bank 1 week after Hato (Figures 4c and 4g), and 70-m isobath 2 weeks after Hato (Figures 4d and 4h). The surface chlorophyll at PRE nearshore increased greatly 1 week after Hato.

A point-by-point comparison before, during, and after Hato has also been done after interpolating model output to observational sites (Figures S8a–S8d in Supporting Information S1). Before Hato, the surface chlorophyll concentration from the model was in good agreement with observations, as indicated by a high correlation coefficient (0.72), a low bias (0.09), and an RMSD of 0.4. After Hato, while the correlation coefficient reduced ( $\sim 0.5$ ), both the bias ( $\sim 0.49$ ) and RMSD ( $\sim 0.71$ ) increased. A detailed analysis indicates that the overestimation mainly occurred offshore (Figure S5f in Supporting Information S1).

However, it is worth noting that satellite-based surface chlorophyll concentrations derived from remote sensing algorithms applied to ocean color sensors are generally designed for the optical properties of open ocean waters. Applying these algorithms to estuarine and coastal waters often results in poor predictions (Ye et al., 2020). This probably implies that the surface chlorophyll concentrations from satellites may also have a bias. Therefore, the

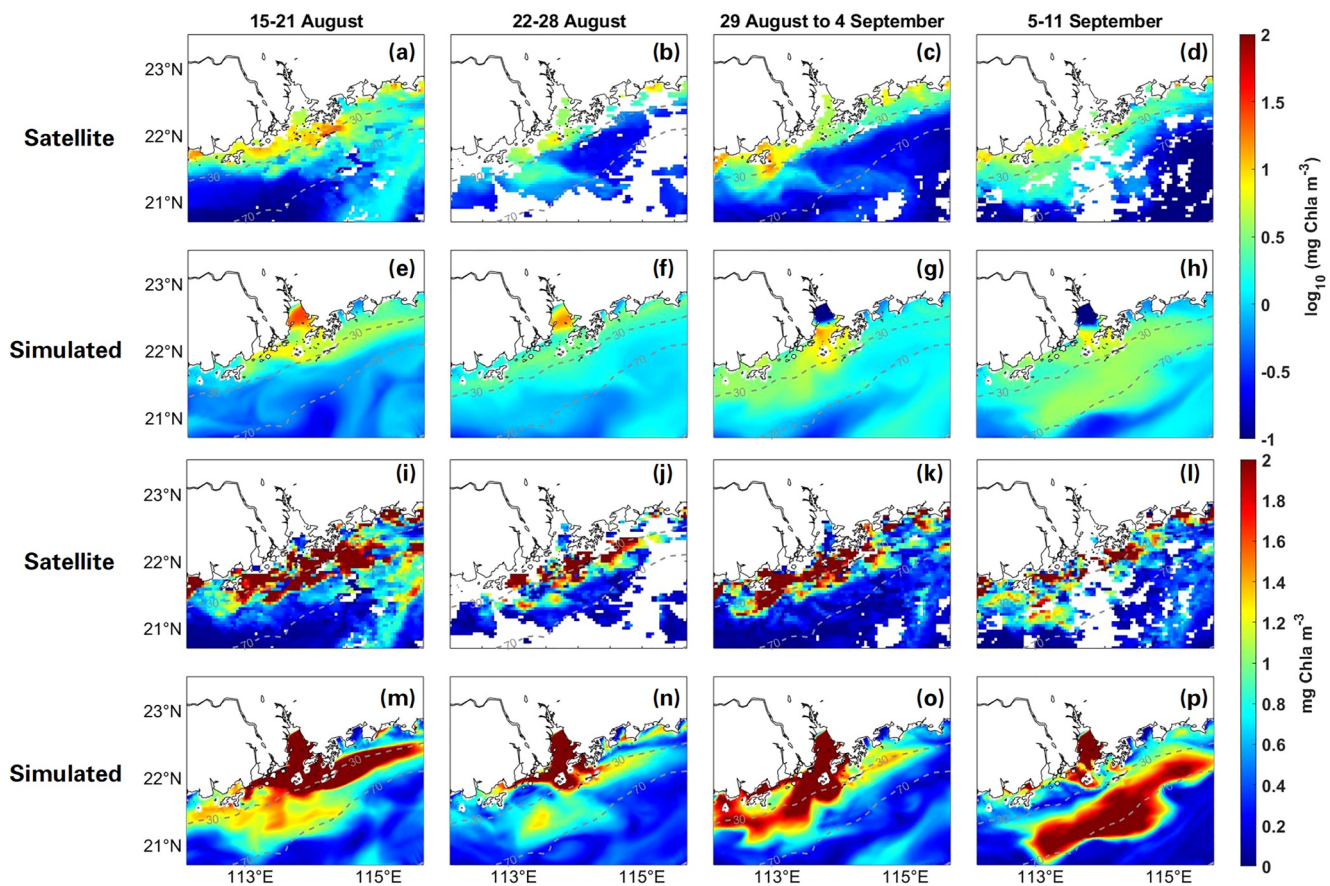


**Figure 4.** Composite of surface chlorophyll concentration (a–h) and deviation (i–p) before (August 15–21) (a, e, i, and m), during (August 22–28) (b, f, j, and n), 1 week after (August 29 to September 4) (c, g, k, and o), and 2 weeks after (September 5–11) (d, h, l, and p) Typhoon Hato. The bathymetry for nearshore (30 m) and offshore separation (70 m) were added as gray dashed lines.

comparison with satellite-based surface chlorophyll cannot accurately represent the bias in the model. Though we do not have in situ observed surface chlorophyll during Typhoon Hato, some data collected during the June 2017 cruise correspond to a period that is immediately after Typhoon Merbok (Figure S8e in Supporting Information S1). Though not synchronized, the simulation results 4–5 days after Hato and the cruise data 4–5 days after Merbok are highly correlated (0.77) with a low bias (0.28) and RMSD (0.43) (Figure S8f in Supporting Information S1).

Since both model and satellite observations have a bias, we also compare the deviation of surface chlorophyll concentration (Figures 4i–4p). The results reveal similar spatio-temporal variability. During Hato, the high surface chlorophyll water is distributed closer to the Lingding Bay (Figures 4j and 4n). It spreads to the nearshore region 1 week after Hato and the offshore region 2 weeks after Hato (Figure 4k, 4l, 4o, and 4p). The goal of our work is to quantitatively estimate the potential mechanisms driving the variability of phytoplankton that has been identified from satellite observations in previous research. The consistency in deviations indicates that differences between simulated and satellite-observed chlorophyll will not impact our discussion significantly.

### 3.2. Spatio-Temporal Variability of Phytoplankton Distribution Under Hato

Satellite data show that high chlorophyll concentration co-occurs with low salinity during the simulation period. However, the satellite product poorly resolves the nearshore plume region, and the data resolution was coarse for the PRE and adjacent seas. Besides, satellite observations of surface chlorophyll in shallow waters during and after the passage of storms are affected significantly by the presence of clouds. Since in situ data are rarely available for strong typhoon cases such as Hato, our modeling system could serve as an important tool for testing

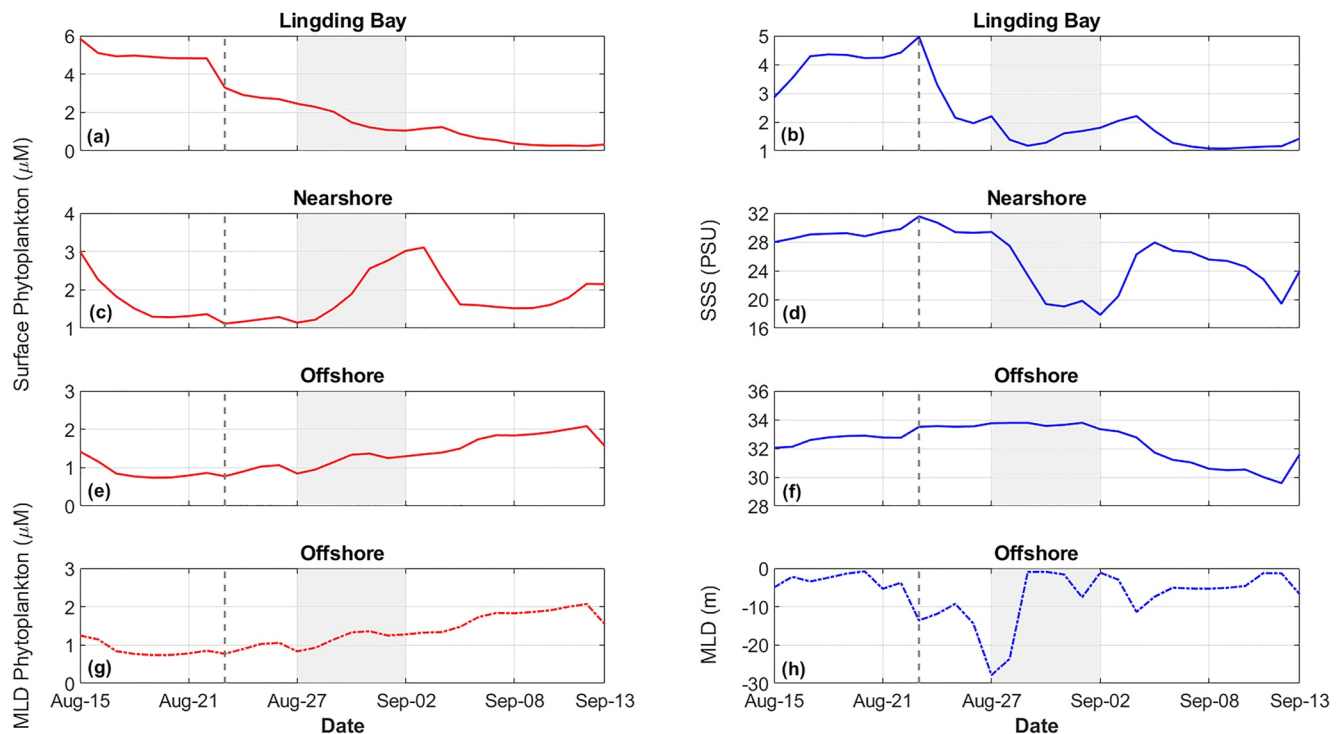


**Figure 5.** The simulated phytoplankton biomass, sea surface salinity (SSS), and mixed layer depth (MLD). (a, b) The averaged surface phytoplankton biomass and SSS within the Lingding Bay; (c, d) the averaged surface phytoplankton biomass and SSS nearshore; (e, f) the averaged surface phytoplankton biomass and SSS offshore; (g) the averaged phytoplankton biomass within offshore MLD; (h) the offshore MLD. The boxes over which the averages were calculated for the Lingding Bay, nearshore and offshore regions are shown in Figure 1. The gray shaded area highlights the timing of runoff increase due to the heavy rainfall.

various hypotheses about phytoplankton biomass and primary production across the ecological gradient from the Lingding Bay, via the nearshore, to the adjacent offshore region.

In the following, we first averaged the simulated phytoplankton biomass and SSS over the three selected regions to discern their evolutions (Figures 5a–5f). Within Lingding Bay, the phytoplankton biomass started at about  $5.8 \mu\text{M}$  ( $\text{mmole-N/m}^3$ ) and dropped to  $3.3 \mu\text{M}$  during Hato's passage (Figure 5a). Meanwhile, SSS increased from 2.9 to 5 PSU (Figure 5b). This asymmetry was caused by strong vertical mixing, which entrains subsurface high-salinity and low-biomass seawater into the surface layers. After Hato, the phytoplankton biomass decreased gradually to  $1 \mu\text{M}$  with a slightly increase to  $1.2 \mu\text{M}$  2 weeks after (September 4). Meanwhile, SSS dropped to 1 PSU on August 29 after Hato and increased to 2 PSU 2 weeks later. For the nearshore region, the phytoplankton biomass started at about  $3 \mu\text{M}$  and decreased to about  $1 \mu\text{M}$  on August 23 during Hato's passage (Figure 5c). It remained at low levels for 5 days and increased afterward. Subsequently, the phytoplankton biomass increased by  $3 \mu\text{M}$  over the 2-week period following Hato (September 3). Meanwhile, the SSS in the nearshore started at about 28 PSU and increased to about 32 PSU on August 23 during Hato's passage (Figure 5d). Subsequently, it reduced to 29 PSU and remained at this level until August 26. Next, the SSS dropped rapidly to 18 PSU until September 2 and increased to about 28 PSU 2 weeks later. For the offshore region, phytoplankton concentration began at about  $1.4 \mu\text{M}$  and remained below  $1 \mu\text{M}$  until August 23 (Figure 5e). After the passage of Hato, it increased gradually to over  $2 \mu\text{M}$  by September 10 with two sharp increases on August 26 and 31. The offshore SSS was 33.5 PSU on August 23 and decreased to below 30 PSU by September 10 (Figure 5f). While the correlation coefficient between the time series of surface phytoplankton biomass and SSS is positive (0.87) within Lingding Bay, it becomes negative nearshore ( $-0.7$ ) and offshore ( $-0.8$ ).

Vertical mixing, entrainment, and upwelling have been recognized as processes that play an important role in triggering surface phytoplankton blooms after typhoons in the offshore region of the northern SCS. However, we wondered if the surface phytoplankton biomass was mainly due to the upward mixing of nutrients from the deep water into the ocean surface or because surface entrainment of deep chlorophyll maxima. We therefore examine the averaged phytoplankton biomass within the MLD for the offshore region next. If the supply of nutrients did



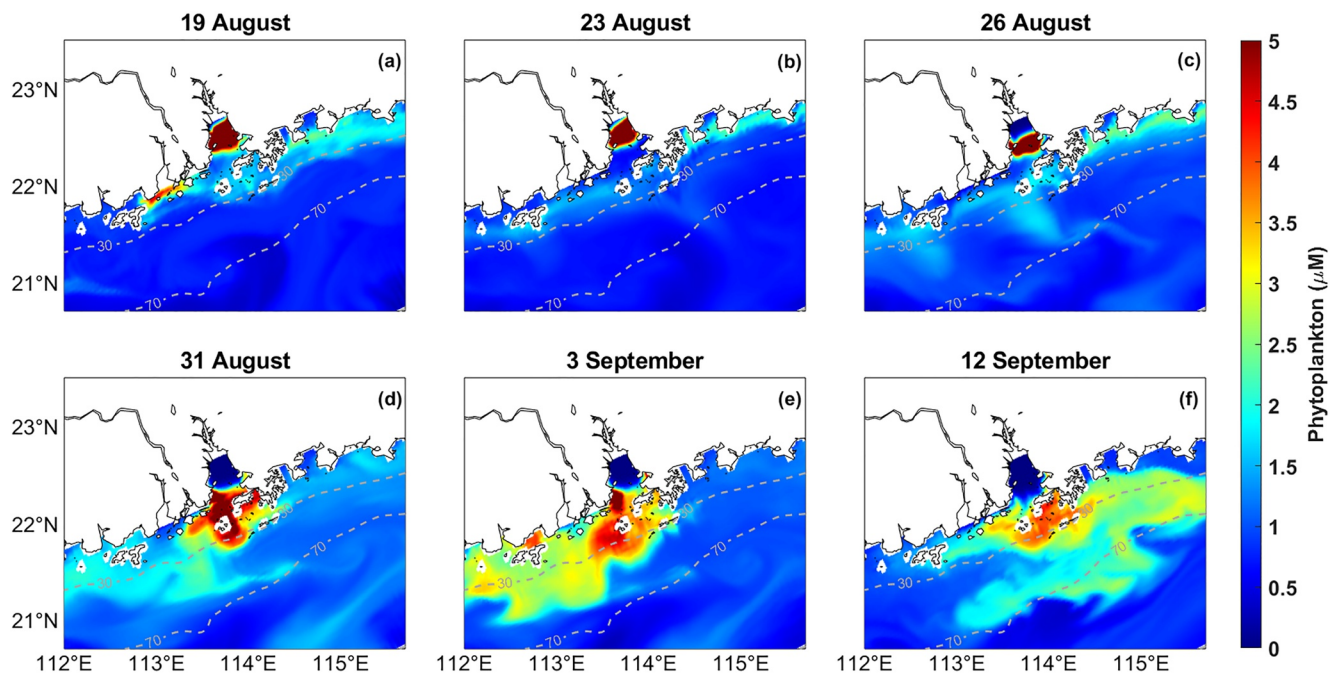


**Figure 6.** Snapshots of simulated surface phytoplankton biomass on August 19 (before Hato); August 23 (during Hato); August 26 (within 1 week); August 31 (within 1–2 weeks); September 3 (2 weeks), and September 12 (3 weeks). Units:  $\mu\text{M}$  ( $\text{mmole-N/m}^3$ ). The isobaths demarking the nearshore (30 m) and offshore (70 m) regions have been added as gray dashed lines.

not play an important role, we would expect the averaged phytoplankton biomass within the MLD would differ from the surface phytoplankton concentration substantially. The MLD is estimated as the depth where the density increases with respect to its value near the surface by  $0.03 \text{ kg/m}^3$  (de Boyer Montégut et al., 2004). Starting at 5 m, the MLD deepened to 13.6 m on August 23, and increased further to 27.8 m by August 27 (Figure 5h). Subsequently, the MLD shoaled to about 1 m rapidly on August 29. After that, the MLD deepened to about 11.4 m on September 4, and then shoaled to about 5 m on September 6, where it remained until September 10. The averaged phytoplankton biomass within the MLD for the offshore region differs slightly from the surface value (Figure 5g). They both drop slightly on August 27 although the overall trend is positive. The above results suggest that the upward of nutrients into ocean surface played a dominant role in stimulating the primary production after typhoon, while surface entrainment of deep chlorophyll maxima played a minor role.

For a better understanding of the associated change in biophysical conditions, we next consider snapshots of surface and cross-sectional phytoplankton along with nitrate concentration, salinity, temperature, velocity, and eddy viscosity before (August 19), during (August 23), within 1 week (August 26), 1 week (August 31), 2 weeks (September 3), and 3 weeks (September 12) after Hato (Figures 6–9). Figure 6 shows that the surface phytoplankton biomass concentrations were high within Lingding Bay, moderate next to the coast, and extremely low in the offshore region before, during, and within 1 week after Hato's passage. In contrast, the phytoplankton biomass reduced greatly within Lingding Bay, but increased near the mouth of the Bay on August 31. The phytoplankton biomass continued increasing near the western bank 2 weeks later along with high concentrations near the eastern bank and offshore region 3 weeks after Hato.

Before Hato, although the surface phytoplankton biomass was low, the subsurface phytoplankton increased downwards between 10 and 40 m from near-to offshore, forming the deep phytoplankton maximum (DPM) right above the high  $\text{NO}_3$  concentration water (Figure 7a). On August 23 and within 1 week, the DPM vanished, and high phytoplankton biomass was present throughout the water column in the nearshore region (Figures 7b–7c). One week after Hato, the high phytoplankton biomass water extended from 17 to 40 km offshore and in the upper-10 m. The offshore extension was accompanied by high riverine  $\text{NO}_3$ , which supports the high phytoplankton growth rate in this region (Figures 7d–7e). In addition, we also observed high phytoplankton biomass around 65 km offshore and detached from the nearshore signal. The detached phytoplankton biomass reaches a value as high as  $2.4 \mu\text{M}$  3 weeks after Hato (Figure 7f).

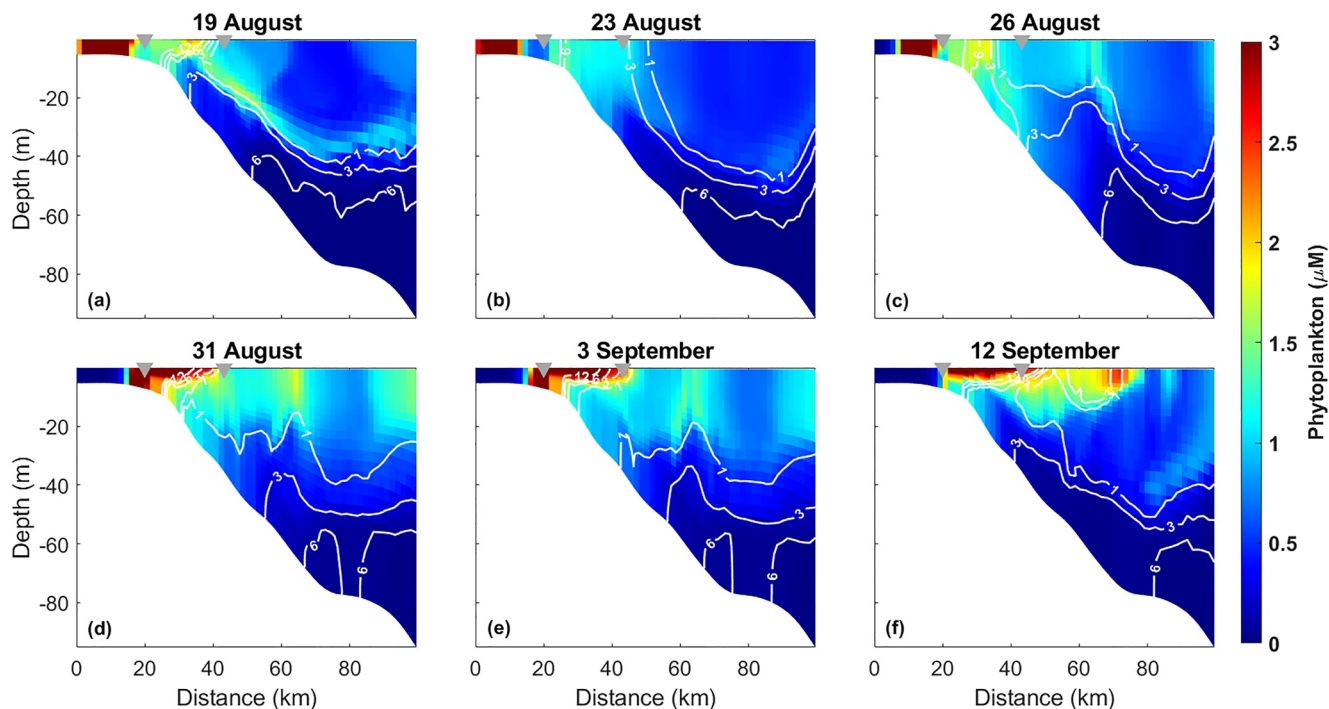


**Figure 7.** Snapshots of simulated phytoplankton biomass (background color) and nitrate concentrations (contours) along the cross-section from Lingding Bay to the offshore region (see Figure 1) on August 19 (before Hato); August 23 (during Hato); August 26 (within 1 week); August 31 (within 1–2 weeks); September 3 (2 weeks) and September 12 (3 weeks). Contour units:  $\mu\text{M}$  ( $\text{mmole-N}/\text{m}^3$ ). The gray triangles on top indicate the separation between the Lingding Bay, nearshore, and offshore regions.

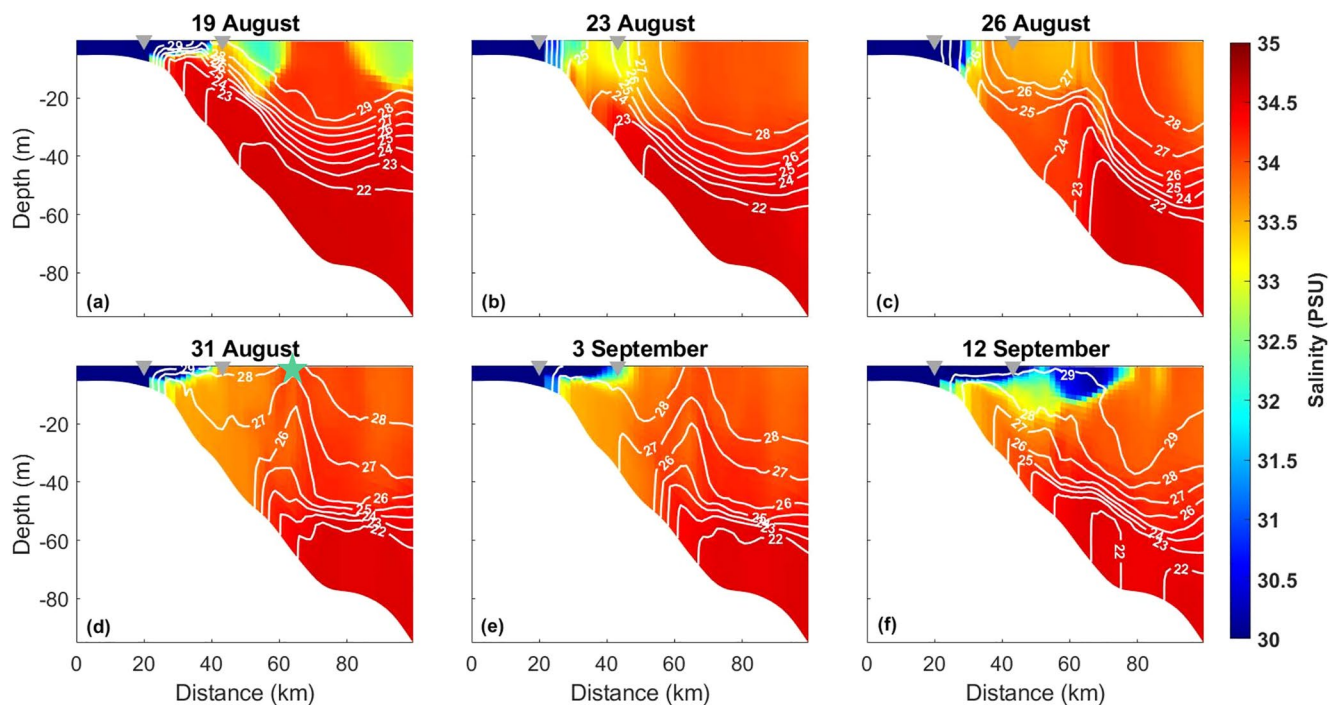


**Figure 8.** Snapshots of simulated salinity (background color) and temperature (contours) along the cross-section from Lingding Bay to offshore (see Figure 1) on August 19 (before Hato); August 23 (during Hato); August 26 (within 1 week); August 31 (within 1–2 weeks); September 3 (2 weeks) and September 12 (3 weeks). Contour units:  $^{\circ}\text{C}$ . The gray triangles on top noted the separation between the Lingding Bay, nearshore, and offshore region. The green star shows the location of time series of temperature in Figure S10 in Supporting Information S1.



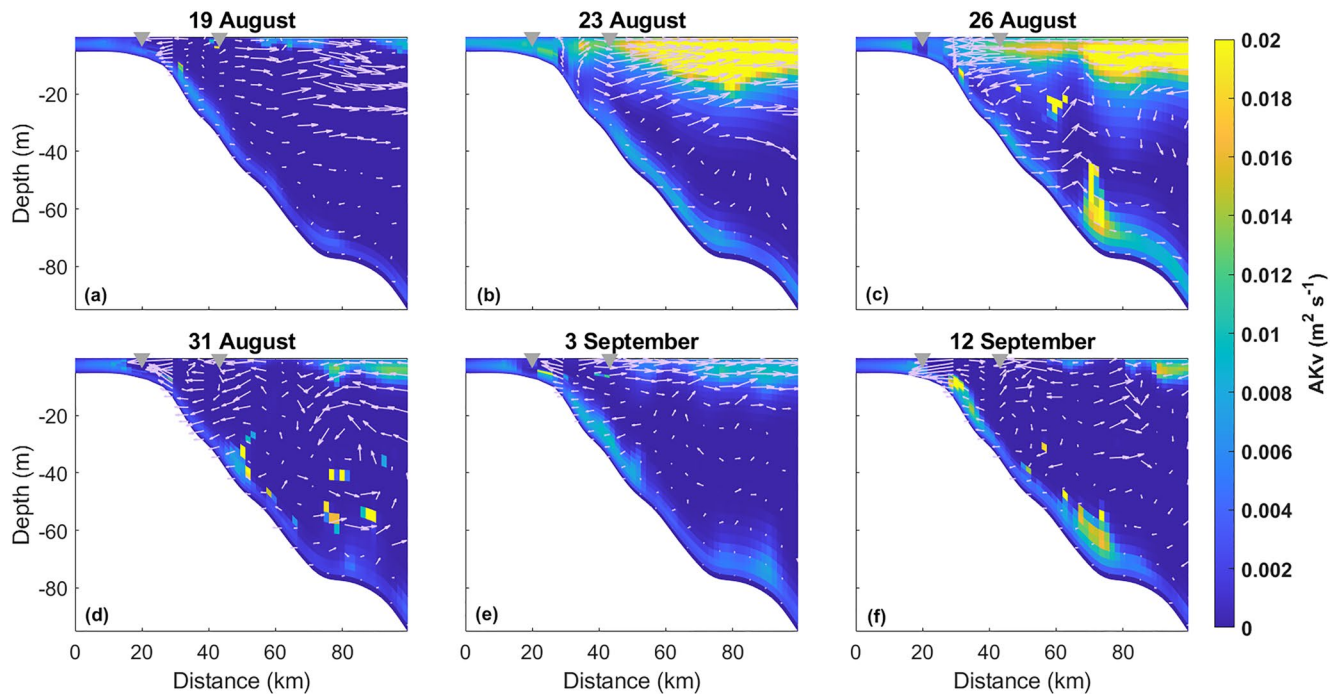


**Figure 9.** Snapshots of simulated eddy viscosity (AKv; background color) and velocity (arrows, contours) along the cross-section from Lingding Bay to offshore (see Figure 1) on August 19 (before Hato); August 23 (during Hato); August 26 (within 1 week); August 31 (within 1–2 weeks); September 3 (2 weeks) and September 12 (3 weeks). Contour units:  $\text{m s}^{-1}$ . The gray triangles on top noted the separation between the Lingding Bay, nearshore, and offshore region. The vertical velocity has been enlarged  $10^3$  times more than the original.

### 3.3. Response of Physical Fields to Hato

Next, we examined vertical cross-sections of salinity, temperature, eddy viscosity, and currents, which can help our understanding of the underlying drivers for the phytoplankton response discussed earlier (Figures 8 and 9). On August 19, before Hato, the model simulated river plume within the Lingding Bay reached the bottom of the water column and extended from 17 to 60 km in the upper-layers nearshore. The thermocline tilted upward toward the surface, dividing the plume into two regions approximately near 45 km (Figure 8a). The currents were offshore, and vertical mixing was small (Figure 9a). The plume water within the Lingding Bay and the nearshore region is collocated with high phytoplankton biomass water. The subsurface DPM was aligned with the 23 PSU isotherm (Figure 7a).

During Hato and within 1 week of its passage, the low salinity plume water was well-mixed throughout the water column within the Lingding Bay and the nearshore region (Figures 8b–8c). The isotherm is stretched vertically, and vertical mixing was large in the top 10 m. The surface currents were offshore on August 23, and turned onshore on August 26 (Figures 9b–9c). The high phytoplankton biomass water was mostly confined within the Lingding Bay and the nearshore region (Figures 7b–7c). On August 26, the vertical mixing was high between 60 and 70 km offshore (below 40 m), where strong upwelling occurred (Figure 9d). It was also where the subsurface nitrate-rich cold water upwelled, and the detached offshore bloom happened (Figures 7c and 8c).

One to two weeks after Hato, we observed that the plume water extends 40–50 km offshore in the top 10 m (Figures 8c–8e). The 26°C, 27°C, and 28°C isotherms were uplifted 60–70 km offshore. Besides, we observed that the eddy viscosity reduced greatly in the upper layers (Figure 9c). The surface currents became onshore on August 31 and offshore on September 3 (Figures 9d–9e). Again, the subsurface nitrate-rich cold water upwelled and detached offshore.

Three weeks after Hato, the plume water extended farther offshore to 75 km (Figure 8f). The temperature and nitrate patterns recovered to pre-typhoon conditions. A low salinity water mass was around 60 km, detached from the main plume. The eddy viscosity was low, and the surface currents returned onshore (Figure 9f). The detached plume water was also where surface high phytoplankton biomass occurred offshore (Figure 7f).

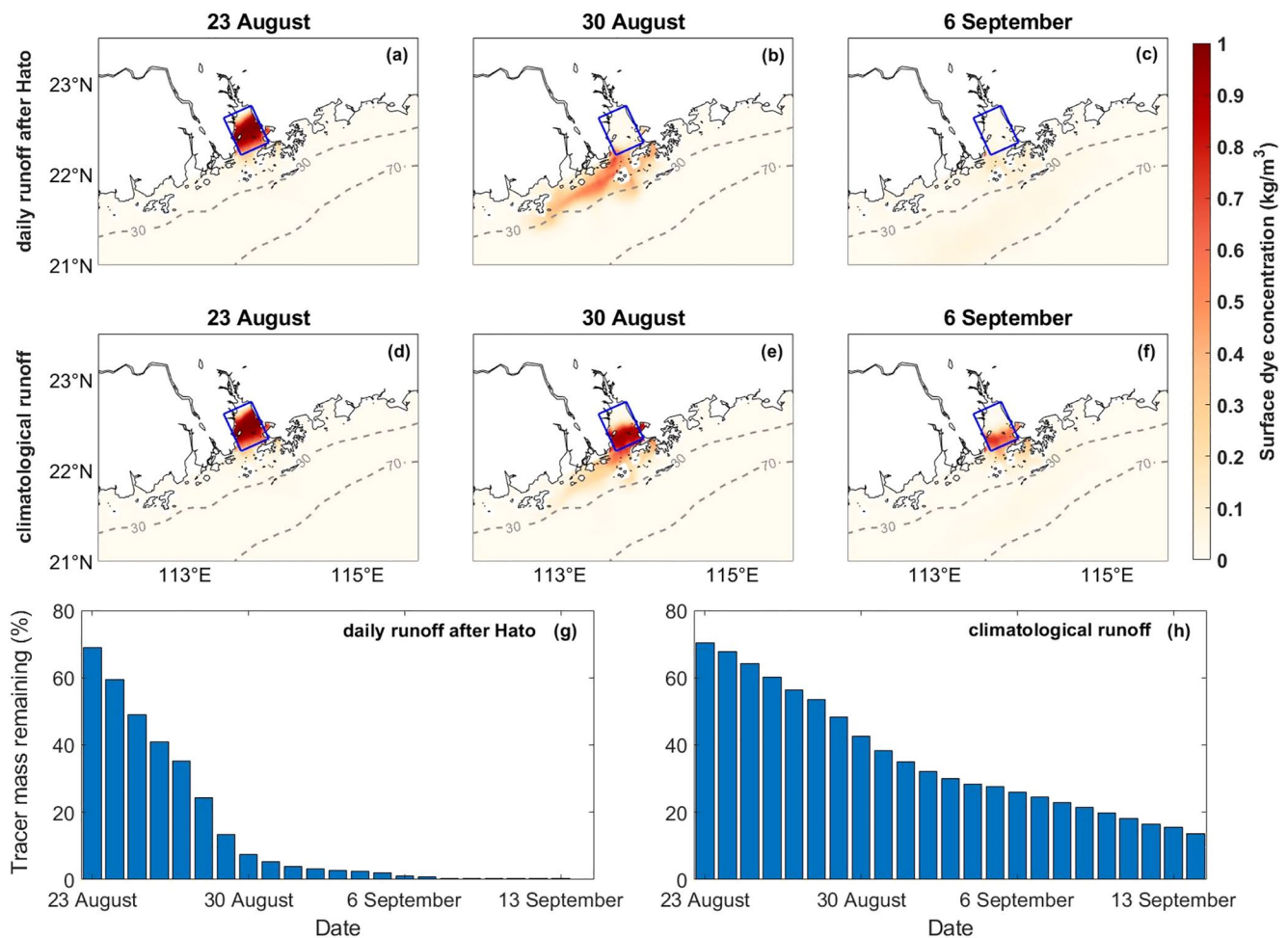


**Figure 10.** The evolution of passive tracer concentrations within the Lingding Bay in passive tracer experiments (a, b, and c for daily runoff; d, e, and f for climatological runoff). Histograms of daily averaged tracer mass remaining in the control volume over time for the daily (g) and climatological (h) runoff experiments. The concentration snapshots start on August 23, 2017 since they were the same before that. The passive tracers were released instantaneously into the Lingding Bay on August 23, 2017 for both experiments. The gray isolines are for isobath 30 and 70 m.

In summary, the high phytoplankton biomass water within the Lingding Bay and the nearshore region, before and after Hato, are aligned with river plume water. While the subsurface high phytoplankton biomass water on August 19 and the detached phytoplankton bloom offshore is aligned with isotherms within 2 weeks, and with plume water after 3 weeks. This suggests that the increased Pearl River discharge and nutrients after rainfall contribute to the enhanced phytoplankton biomass and the chlorophyll bloom within the Lingding Bay and the nearshore region. The phytoplankton bloom offshore is triggered by an increase of nutrients through mixing, entrainment, and upwelling within the first 2 weeks after Hato and is nourished by riverine water subsequently.

### 3.4. Tracer Concentration and Residence Time of Water Mass

To quantify how much the residence time of Lingding Bay can be changed by the sudden runoff increase after Hato, passive tracers are released within Lingding Bay with SWAT daily and climatological runoff forcings, respectively (Figure 10). After Hato, most tracers spread within the 30-m isobath after leaving the Lingding Bay in both experiments. One week after Hato, the tracer concentrations within Lingding Bay in the experiment forced by the daily runoff are lower than in the experiment forced by the climatological runoff (Figures 10b and 10e). In contrast, the tracer concentration between the mouth of the Bay and the 30 m isobath is higher. Almost all tracers leave the Lingding Bay within 2 weeks after Hato in the experiment with daily river forcing (Figure 10c). Further calculations reveal that the water mass residence time was 15 days for the simulation forced with daily

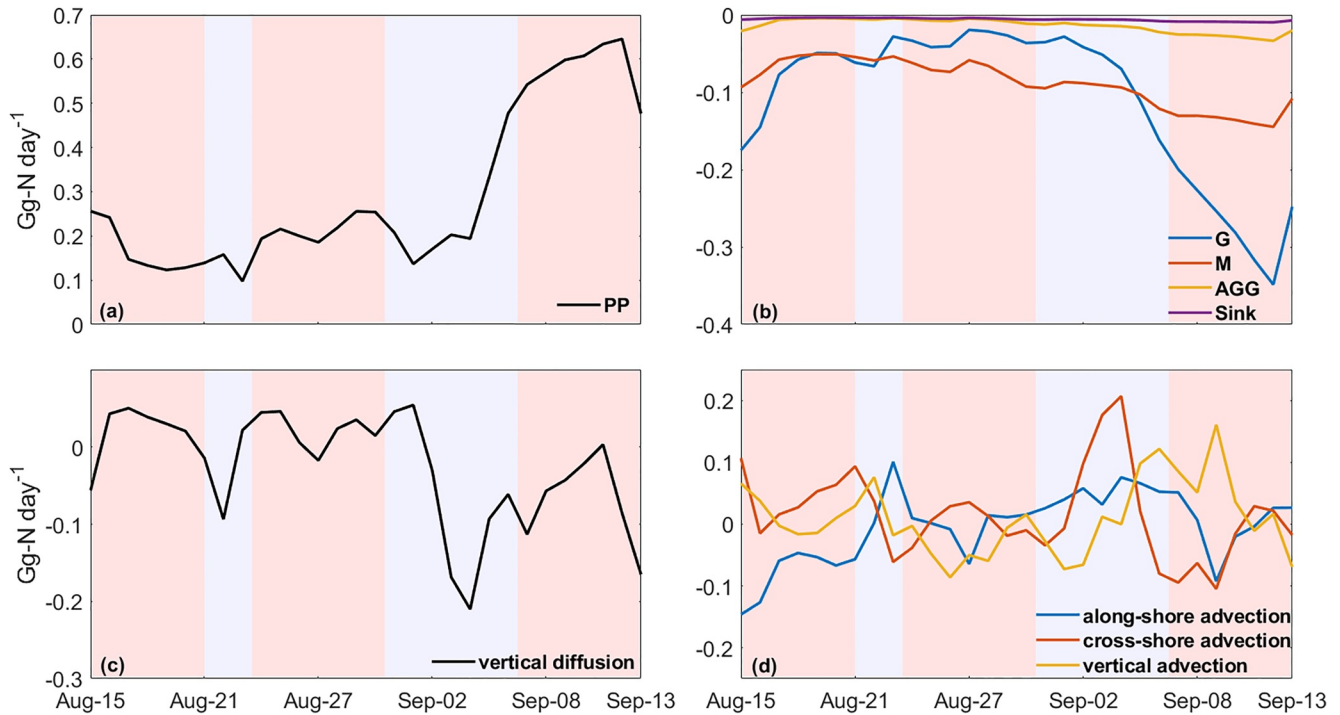


**Figure 11.** Model-estimated daily source and sink terms of surface phytoplankton biomass for the offshore region. The alternating red-blue background color highlights the before, during, 1 week, 2 weeks, and 3 weeks later periods corresponding to Hato's passage in Table 2.

runoff and over 1 month for the simulation forced with climatological runoff. And the decay rate of water mass was  $0.07 \text{ days}^{-1}$  with daily runoff, doubling the run with climatological runoff ( $0.14 \text{ days}^{-1}$ ), respectively. The above results suggest that the low phytoplankton biomass within Lingding Bay after Hato was primarily because the residence time was greatly shortened by the Typhoon-induced heavy rainfall.

### 3.5. The Mass Budget of Surface Phytoplankton

The phytoplankton increase by PP was about 172 kg per day before Hato (Figure 11a). This increase in phytoplankton due to PP was reduced by about 23% during Hato, but enhanced by about 27% during the week after Hato (Table 2). The additional increase was due to the upwelling of subsurface nutrient-rich waters. Much of the

**Table 2**

*The Source and Sink Terms of Surface Phytoplankton Biomass During, 1 Week, 2 Weeks, and 3 Weeks After Hato (Unit: kg-N/day)*

		During Hato (8.21–8.23)	1 week after Hato (8.24–8.30)	2 weeks after Hato (8.31–9.6)	3 weeks after Hato (9.7–9.13)
Biological process	Primary Production (PP)	$131.6 \pm 30.8$	$217.6 \pm 27.9$	$245.9 \pm 118.9$	$582.1 \pm 58.3$
	Grazing (G)	$-52.1 \pm 20.9$	$-31.4 \pm 9.0$	$-71.4 \pm 48.7$	$-267.8 \pm 51.7$
	Mortality (M)	$-55.7 \pm 2.8$	$-72.0 \pm 11.6$	$-97.0 \pm 12.0$	$-131.8 \pm 11.8$
	Aggregation (AGG)	$-5.4 \pm 0.8$	$-7.4 \pm 2.2$	$-14.8 \pm 3.8$	$-27.2 \pm 4.3$
	Sinking (Sink)	$-3.7 \pm 0.2$	$-4.8 \pm 0.8$	$-6.5 \pm 0.8$	$-8.8 \pm 0.8$
Physical process	Alongshore adv.	$15.5 \pm 79.7$	$-2.8 \pm 28.4$	$50.2 \pm 18.3$	$-0.6 \pm 46.7$
	Crossshore adv.	$23.5 \pm 78.4$	$2.5 \pm 26.4$	$54.6 \pm 108.9$	$-34.9 \pm 53.5$
	Vertical adv.	$29.3 \pm 47.0$	$-33.7 \pm 36.6$	$9.5 \pm 75.7$	$38.7 \pm 73.1$
	Vertical diff.	$-28.7 \pm 59.0$	$22.0 \pm 22.9$	$-66.1 \pm 100.3$	$-68.7 \pm 57.4$

increase in phytoplankton biomass is lost to zooplankton grazing and phytoplankton mortality. The amount lost to mortality is higher than grazing during, 1 week, and 2 weeks after Hato.

The net primary production (NPP) represents the rate of accumulation of phytoplankton biomass. We calculate it by removing zooplankton grazing and phytoplankton mortality from the gross primary production. During Hato's passage, the NPP was about 24 kg per day, smaller than the amount lost to the vertical mixing (29 kg per day). The NPP was as high as 114 kg per day 1 week after Hato, much higher than the source and sink terms from multiple physical processes. In contrast, the NPP was about 78 kg per day 2 weeks after Hato, smaller than the amount supplied by horizontal advection, including both the along- and cross-shore components (105 kg per day). It is noteworthy that the gross primary production 3-week after Hato was three times higher than that before Hato. However, different from 1 week and 2 weeks after Hato, the phytoplankton biomass lost due to zooplankton grazing is two times higher than that due to phytoplankton mortality, indicating the ecosystem converted from being a bottom-up control process to a top-down control process.

#### 4. Discussion and Conclusions

While extensive studies have been done on the biophysical response to hurricanes in the open ocean (Chai et al., 2021; Da et al., 2021; Gierach et al., 2009; Gierach & Subrahmanyam, 2008; Lin, 2012; G. Qiu et al., 2021), few studies paid attention to the response of the shallow ocean water in coastal regions, where more complicated atmosphere, hydrodynamic, sediment and ecosystem processes interact (N. Chen et al., 2018; Glenn et al., 2016; Y. Liu et al., 2019; Z. Zhang et al., 2019). Here, the phytoplankton response to Typhoon Hato (2017), a Category 3 TC, was studied using a realistic, three-dimensional (3D), land-ocean-atmosphere modeling system with marine ecosystem and sediment components for the PRE. The comprehensive modeling system reproduced the satellite-observed variability of sea surface salinity and chlorophyll before, during, and after Hato's passage. The passive tracer experiments showed that high river discharge induced by heavy rainfall from the storm doubled the decay rates and halved the residence time. The freshwater pulse washed out the phytoplankton biomass within the Lingding Bay, resulting in a positive relationship between SSS and phytoplankton biomass during the 1-month simulation period.

Figure 12 summarizes the predominant mechanisms regulating the spatio-temporal variability of phytoplankton biomass in and near the PRE during the extreme weather event. The phytoplankton biomass was washed out by the river discharge within the Lingding Bay during the whole simulation period, while it shows strong spatio-temporal variability nearshore and offshore regions during and after Hato. During Hato's passage, the strong vertical mixing confines the low-salinity, high-nutrient water within the Lingding Bay, resulting in lower phytoplankton biomass for the nearshore and offshore regions. One week after Hato, the freshwater is released again, which increases the available nutrients for the nearshore region promoting the phytoplankton biomass there. The vertical mixing and upwelling were strong in the offshore region, increasing phytoplankton biomass significantly. Two weeks after Hato, the increased nutrient availability associated with the significant runoff increase elevated the phytoplankton within the Lingding Bay and the nearshore region. The strong offshore currents advect the high phytoplankton biomass water seawards. The advection of nutrients was responsible for high primary production in the third week. However, the total biomass increase was low due to the top-down pressure from zooplankton grazing.

Our modeling system shows strong upwelling within 1 week after Hato in the offshore region. To examine if the presence of upwelling is a real physics process instead of model artifact, we checked the Aqua/MODIS sea surface temperature (SST) as well as the reanalysis temperature from Hybrid Coordinate Ocean Model (HYCOM). Though with poor spatial coverage, the Aqua/MODIS SST was as high as 31°C before Hato (August 20). It reduced to 29°C 1 week (August 26) after Hato and bounced back to 30°C 3 weeks after (September 10) (Figure S9 in Supporting Information S1). The SST decrease on August 26 is consistent with our simulation. The 3D temperature in our simulation at 60-km offshore indicates that the thermocline shoaled rapidly after Hato, leading to a low surface temperature until September 4 (Figure S10 in Supporting Information S1). Even though the temperature was higher in HYCOM reanalysis relative to our model simulation, the SST decreased after Hato was also present. All of the above results suggest that strong upwelling existed right after the eye passage in the offshore region, which was possibly induced by the cyclonic wind field in the southwest quadrant of the storm.



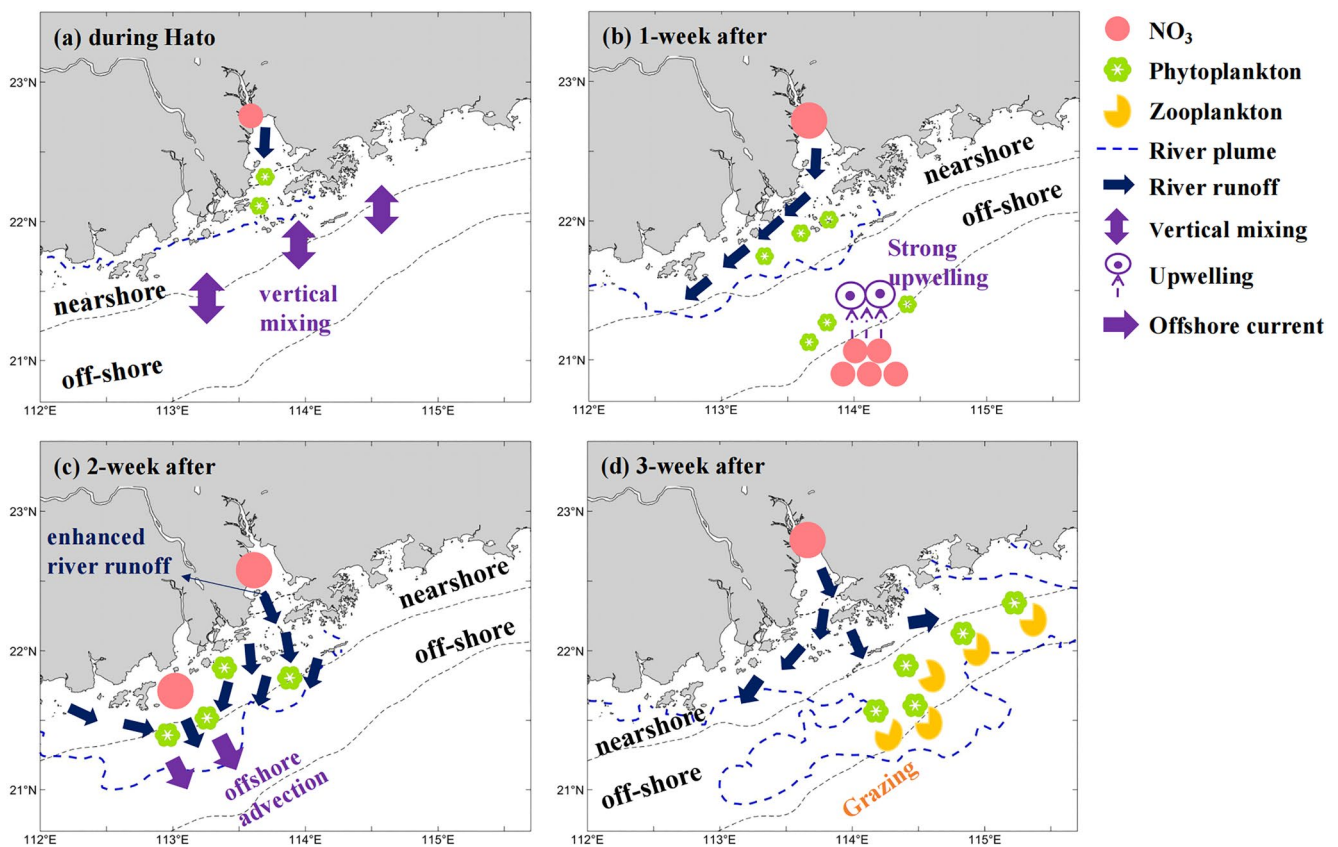


**Figure 12.** Schematic diagram for the response of phytoplankton to Typhoon Hato during the 1-week, 2-week, and 3-week period after Hato.

Previous studies at different estuarine and coastal regions observed that heavy storm-induced precipitation increases river runoff, which then moves the salinity gradient, inorganic nutrients, and organic matter seaward after the storm (Bianucci et al., 2018; Herbeck et al., 2011). Herbeck et al. (2011) investigated the change in hydrological and biogeochemical conditions near the Wenchang/Wenjiao Estuary (WWE) on the tropical island of Hainan, China, before and after typhoon Kammuri in August 2008 using in situ observations. Their results suggest that the uptake of excess nutrients inside the lagoon was inhibited because of reduced water transparency and lack of phytoplankton, which has been washed out by the initial freshwater pulse. Two weeks after the typhoon, the biogeochemical characteristics are still different from pre-typhoon conditions. Bianucci et al. (2018) used a diverse suite of data sets for the northern Gulf of Mexico and found that a few days after Hurricane Rita's passage, the elevated consumption of dissolved oxygen was associated with an increase in organic matter. The environmental context for our modeling simulation was identical to that of Herbeck et al. (2011) and Bianucci et al. (2018) by providing a quantitative measure of the relative importance of different processes.

Although our modeling system captures the general spatio-temporal variability of satellite-based sea surface salinity and chlorophyll, it overestimates their magnitude. A further comparison with in situ data shows that the simulated sea surface salinity and temperature are closer to the observed, but the simulated surface chlorophyll field has a positive bias relative to the observation (Figures S6 and S7 in Supporting Information S1).

The differences can partially originate from satellite observations. But more importantly, there are still many limitations to the current biogeochemistry model setup and parameterization schemes used, including (a) the PRE is known as a phosphate-limitation system during summer (Gan et al., 2014; Yin et al., 2004; Yu & Gan, 2022), while the effect of phosphorus-limitation has not been incorporated in the current version of water-column biogeochemistry model; (b) the impact of sediment processes on phytoplankton growth is not only limited to altering light attenuation, but also to nutrient regeneration through complicated biogeochemical processes; and (c) the land module in our modeling system is limited only in generating the fresh river runoff, while typhoon-induced soil erosion may increase the contribution of terrestrial organic matter and inorganic nutrients. Finally, the riverine



inorganic suspended sediment (ISS) is also an important term to reduce the light attenuation in the marine ecosystem model, which was not incorporated in the current model (Feng et al., 2015).

The current study aims to investigate the potential mechanisms driving the variability of phytoplankton observed by satellites quantitatively. The bias of simulated results will not impact the overall discussion on the relative amount of phytoplankton biomass altered by multiple processes. To further improve the modeling system and to make it more realistic, it may be worth implementing the hydrodynamic-sediment transport-biogeochemical model for this region, which links the CSTMS, water column biogeochemistry model, and the seabed diagenetic model (Moriarty et al., 2017, 2018, 2021). It will also be necessary to include a process-based land ecosystem model in future modeling efforts to incorporate land biogeochemistry and ISS (Tian et al., 2015; Yao et al., 2021). However, constructing a more comprehensive modeling system requires additional observational data to improve model parameterization schemes and for validation of the model. We believe future advanced observational techniques, especially autonomous surface vehicles that could be adapted to extreme weather conditions, such as Bio-Argo, Wave Glider, and Sail-drone (Chai et al., 2021), will be helpful in verifying the hypothesis presented in this study and for further improving the accuracy of model simulations in future.

## Data Availability Statement

Both the ocean color and sea surface salinity used for the model-observation comparison are publicly available from the website. For the GlobColour, data were available from <https://hermes.acri.fr/>. For SMAP Level 3, data were available from [https://data.remss.com/smap/SSS/V04.0/FINAL/L3/8day\\_running/](https://data.remss.com/smap/SSS/V04.0/FINAL/L3/8day_running/). Both SWAT and COAWST were open source software. The SWAT code can be downloaded from <https://swat.tamu.edu/software/swat-executables/>. The version of COAWST code with all observational, satellite, and model data used in this research has been uploaded to Zenodo <https://doi.org/10.5281/zenodo.6806149>.

## Acknowledgments

This study was supported by the Southern Marine Science and Engineering Guangdong Laboratory (Guangzhou) (Grant GML2019ZD0303), the National Natural Science Foundation of China (41890851), the State Key Laboratory of Tropical Oceanography Independent Research Fund (Grant LTOZZ2103), the State Key Laboratory of Tropical Oceanography, South China Sea Institute of Oceanology, Chinese Academy of Sciences (Grant LTO2102), and the National Natural Science Foundation of China (Grant 42077057). The authors sincerely thank Dr. Wenping Gong and Dr. Heng Zhang at Sun-Yan-Sen University and Dr. Yuren Chen at Horn Point Laboratory, University of Maryland helped with CSTMS and SWAN run. The authors also thank Dr. Hui Wu at East China Normal University for tracer experiments design. Dr. Karthik Balaguru was supported by the Office of Science (BER) of the U.S. Department of Energy as part of the collaborative, multi-program Integrated Coastal Modeling (ICoM) project. The Pacific Northwest National Laboratory is operated for DOE by Battelle Memorial Institute under contract DE-AC05-76RL01830. The authors thank use of the HPCC at the South China Sea Institute of Oceanology, Chinese Academy of Sciences.

## References

- Balaguru, K., Chang, P., Saravanan, R., Leung, L. R., Xu, Z., Li, M., & Hsieh, J.-S. (2012). Ocean barrier layers' effect on tropical cyclone intensification. *Proceedings of the National Academy of Sciences of the United States of America*, 109(36), 14343–14347. <https://doi.org/10.1073/pnas.1201364109>
- Balaguru, K., Foltz, G. R., Leung, L. R., & Emanuel, K. A. (2016). Global warming-induced upper-ocean freshening and the intensification of super typhoons. *Nature Communications*, 7, 13670. <https://doi.org/10.1038/ncomms13670>
- Bianucci, L., Balaguru, K., Smith, R. W., Leung, L. R., & Moriarty, J. M. (2018). Contribution of hurricane-induced sediment resuspension to coastal oxygen dynamics. *Scientific Reports*, 8, 15740. <https://doi.org/10.1038/s41598-018-33640-3>
- Chai, F., Wang, Y., Xing, X., Yan, Y., Xue, H., Wells, M., & Boss, E. (2021). A limited effect of sub-tropical typhoons on phytoplankton dynamics. *Biogeosciences*, 18(3), 849–859. <https://doi.org/10.5194/bg-18-849-2021>
- Chang, Y., Liao, H.-T., Lee, M.-A., Chan, J.-W., Shieh, W.-J., Lee, K.-T., et al. (2008). Multisatellite observation on upwelling after the passage of Typhoon Hai-Tang in the southern East China Sea. *Geophysical Research Letters*, 35(3), L03612. <https://doi.org/10.1029/2007gl032858>
- Chen, N., Krom, M. D., Wu, Y., Yu, D., & Hong, H. (2018). Storm induced estuarine turbidity maxima and controls on nutrient fluxes across river-estuary-coast continuum. *Science of the Total Environment*, 628–629, 1108–1120. <https://doi.org/10.1016/j.scitotenv.2018.02.060>
- Chen, Y., Chen, L., Zhang, H., & Gong, W. (2019). Effects of wave-current interaction on the Pearl River Estuary during Typhoon Hato. *Estuarine, Coastal and Shelf Science*, 228, 106364. <https://doi.org/10.1016/j.ecss.2019.106364>
- Da, N. D., Foltz, G. R., & Balaguru, K. (2021). Observed global increases in tropical cyclone-induced ocean cooling and primary production. *Geophysical Research Letters*, 48(9), e2021GL092574. <https://doi.org/10.1029/2021GL092574>
- de Boyer Montégut, C., Madec, G., Fischer, A. S., Lazar, A., & Ludicone, D. (2004). Mixed layer depth over the global ocean: An examination of profile data and a profile based climatology. *Journal of Geophysical Research*, 109(C12), C12003. <https://doi.org/10.1029/2004jc002378>
- Elsner, J. B., Kossin, J. P., & Jagger, T. H. (2008). The increasing intensity of the strongest tropical cyclones. *Nature*, 455(7209), 92–95. <https://doi.org/10.1038/nature07234>
- Eppley, R. W. (1972). Temperature and phytoplankton growth sea. *Fishery Bulletin*, 70(4), 1063–1085.
- Evans, G. T., & Parslow, J. S. (1985). A model of annual plankton cycles. *Biological Oceanography*, 3(3), 327–347. <https://doi.org/10.1080/01965581.1985.10749478>
- Feng, Y., Friedrichs, M. A. M., Wilkin, J., Tian, H., Yang, Q., Hofmann, E. E., et al. (2015). Chesapeake Bay nitrogen fluxes derived from a land-estuarine ocean biogeochemical modeling system: Model description, evaluation, and nitrogen budgets. *Journal of Geophysical Research: Biogeosciences*, 120(8), 1666–1695. <https://doi.org/10.1002/2015jg002931>
- Fennel, K., Hetland, R., Feng, Y., & DiMarco, S. (2011). A coupled physical-biological model of the Northern Gulf of Mexico shelf: Model description, validation and analysis of phytoplankton variability. *Biogeosciences*, 8(7), 1881–1899. <https://doi.org/10.5194/bg-8-1881-2011>
- Fennel, K., Wilkin, J., Levin, J., Moisan, J., O'Reilly, J., & Haidvogel, D. (2006). Nitrogen cycling in the Middle Atlantic Bight: Results from a three-dimensional model and implications for the North Atlantic nitrogen budget. *Global Biogeochemical Cycles*, 20(3), GB3007. <https://doi.org/10.1029/2005gb002456>
- Fournier, S., & Lee, T. (2021). Seasonal and interannual variability of sea surface salinity near major river mouths of the world ocean inferred from gridded satellite and in-situ salinity products. *Remote Sensing*, 13, 728. <https://doi.org/10.3390/rs13040728>
- Fujii, M., & Yamanaka, Y. (2008). Effects of storms on primary productivity and air-sea CO<sub>2</sub> exchange in the subarctic Western North Pacific: A modeling study. *Biogeosciences*, 5(4), 1189–1197. <https://doi.org/10.5194/bg-5-1189-2008>

- Gan, J., Lu, Z., Cheung, A., Dai, M., Liang, L., Harrison, P. J., & Zhao, X. (2014). Assessing ecosystem response to phosphorus and nitrogen limitation in the Pearl River plume using the Regional Ocean Modeling System (ROMS). *Journal of Geophysical Research: Oceans*, 119(12), 8858–8877. <https://doi.org/10.1002/2014jc009951>
- Geyer, W. R., Morris, J. T., Pahl, F. G., & Jay, D. A. (2000). *Interaction between physical processes and ecosystem structure: A comparative approach* (pp. 177–206). Island Press.
- Gierach, M. M., & Subrahmanyam, B. (2008). Biophysical responses of the upper ocean to major Gulf of Mexico hurricanes in 2005. *Journal of Geophysical Research*, 113(C4), C04029. <https://doi.org/10.1029/2007jc004419>
- Gierach, M. M., Subrahmanyam, B., & Thoppil, P. G. (2009). Physical and biological responses to Hurricane Katrina (2005) in a 1/25 degree nested Gulf of Mexico HYCOM. *Journal of Marine Systems*, 78(1), 168–179. <https://doi.org/10.1016/j.jmarsys.2009.05.002>
- Glenn, S. M., Miles, T. N., Serokal, G. N., Xu, Y., Forney, R. K., Yu, F., et al. (2016). Stratified coastal ocean interactions with tropical cyclones. *Nature Communications*, 7, 10887. <https://doi.org/10.1038/ncomms10887>
- Goldenberg, S. B., Landsea, C. W., Mestas-Nunez, A. M., & Gray, W. M. (2001). The recent increase in Atlantic hurricane activity: Causes and implications. *Science*, 293(5529), 474–479. <https://doi.org/10.1126/science.1060040>
- Guo, X., Song, X., Gao, Y., Luo, Y., Xu, Y., Huang, T., & Wang, L. (2020). Inter-annual variability of the carbonate system in the hypoxic upper Pearl River Estuary in winter. *Frontiers in Marine Science*, 7, 594725. <https://doi.org/10.3389/fmars.2020.594725>
- Herbeck, L. S., Unger, D., Krumme, U., Liu, S. M., & Jennerjahn, T. C. (2011). Typhoon-induced precipitation impact on nutrient and suspended matter dynamics of a tropical estuary affected by human activities in Hainan, China. *Estuarine, Coastal and Shelf Science*, 93(4), 375–388. <https://doi.org/10.1016/j.ecss.2011.05.004>
- Hu, J., Zhang, Z., Wang, B., & Huang, J. (2021). Long-term spatiotemporal variations in and expansion of low-oxygen conditions in the Pearl River estuary: A study synthesizing observations during 1976–2017. *Biogeosciences*, 18(18), 5247–5264. <https://doi.org/10.5194/bg-18-5247-2021>
- Ke, S., Zhang, P., Ou, S., Zhang, J., Chen, J., & Zhang, J. (2022). Spatiotemporal nutrient patterns, composition, and implications for eutrophication mitigation in the Pearl River Estuary, China. *Estuarine, Coastal and Shelf Science*, 266, 107749. <https://doi.org/10.1016/j.ecss.2022.107749>
- Lin, I. I. (2012). Typhoon-induced phytoplankton blooms and primary productivity increase in the Western North Pacific subtropical ocean. *Journal of Geophysical Research*, 117(C3), C03039. <https://doi.org/10.1029/2011jc007626>
- Liu, H., Hu, Z., Huang, L., Huang, H., Chen, Z., Song, X., et al. (2013). Biological response to typhoon in northern South China Sea: A case study of "Koppu". *Continental Shelf Research*, 68, 123–132. <https://doi.org/10.1016/j.csr.2013.08.009>
- Liu, S., Li, J., Sun, L., Wang, G., Tang, D., Huang, P., et al. (2020). Basin-wide responses of the South China Sea environment to super Typhoon Mangkhut (2018). *Science of the Total Environment*, 731, 139093. <https://doi.org/10.1016/j.scitotenv.2020.139093>
- Liu, Y., Tang, D., & Evgeny, M. (2019). Chlorophyll concentration response to the typhoon wind-pump induced upper ocean processes considering air-sea heat exchange. *Remote Sensing*, 11(15), 1825. <https://doi.org/10.3390/rs11151825>
- Lu, F.-H., Ni, H.-G., Liu, F., & Zeng, E. Y. (2009). Occurrence of nutrients in riverine runoff of the Pearl River Delta, South China. *Journal of Hydrology*, 376(1–2), 107–115. <https://doi.org/10.1016/j.jhydrol.2009.07.018>
- Mei, W., Xie, S. P., Primeau, F., McWilliams, J. C., & Pasquero, C. (2015). Northwestern Pacific typhoon intensity controlled by changes in ocean temperatures. *Science Advances*, 1(4), e1500014. <https://doi.org/10.1126/sciadv.1500014>
- Mellor, G. L., & Yamada, T. (1982). Development of a turbulence closure-model for geophysical fluid problems. *Reviews of Geophysics*, 20(4), 851–875. <https://doi.org/10.1029/RG020i004p00851>
- Monsen, N. E., Cloern, J. E., Lucas, L. V., & Monismith, S. G. (2002). A comment on the use of flushing time, residence time, and age as transport time scales. *Limnology & Oceanography*, 47(5), 1545–1553. <https://doi.org/10.4319/lo.2002.47.5.1545>
- Moriarty, J. M., Friedrichs, M. A. M., & Harris, C. K. (2021). Seabed resuspension in the Chesapeake Bay: Implications for biogeochemical cycling and hypoxia. *Estuaries and Coasts*, 44(1), 103–122. <https://doi.org/10.1007/s12237-020-00763-8>
- Moriarty, J. M., Harris, C. K., Fennel, K., Friedrichs, M. A. M., Xu, K., & Rabouille, C. (2017). The roles of resuspension, diffusion and biogeochemical processes on oxygen dynamics offshore of the Rhone River, France: A numerical modeling study. *Biogeosciences*, 14(7), 1919–1946. <https://doi.org/10.5194/bg-14-1919-2017>
- Moriarty, J. M., Harris, C. K., Friedrichs, M. A. M., Fennel, K., & Xu, K. (2018). Impact of seabed resuspension on oxygen and nitrogen dynamics in the Northern Gulf of Mexico: A numerical modeling study. *Journal of Geophysical Research: Oceans*, 123(10), 7237–7263. <https://doi.org/10.1029/2018jc013950>
- Pan, G., Chai, F., Tang, D., & Wang, D. (2017). Marine phytoplankton biomass responses to typhoon events in the South China Sea based on physical-biogeochimical model. *Ecological Modelling*, 356, 38–47. <https://doi.org/10.1016/j.ecolmodel.2017.04.013>
- Pan, J., Huang, L., Devlin, A. T., & Lin, H. (2018). Quantification of typhoon-induced phytoplankton blooms using satellite multi-sensor data. *Remote Sensing*, 10(2), 318. <https://doi.org/10.3390/rs10020318>
- Peng, S., Li, Y., Gu, X., Chen, S., Wang, D., Wang, H., et al. (2015). A real-time regional forecasting system established for the South China Sea and its performance in the track forecasts of tropical cyclones during 2011–13. *Weather and Forecasting*, 30(2), 471–485. <https://doi.org/10.1175/waf-d-14-00070.1>
- Qiu, D., Zhong, Y., Chen, Y., Tan, Y., Song, X., & Huang, L. (2019). Short-term phytoplankton dynamics during typhoon season in and near the Pearl River estuary, South China Sea. *Journal of Geophysical Research: Biogeosciences*, 124(2), 274–292. <https://doi.org/10.1029/2018jg004672>
- Qiu, G., Xing, X., Chai, F., Yan, X.-H., Liu, Z., & Wang, H. (2021). Far-field impacts of a super typhoon on upper ocean phytoplankton dynamics. *Frontiers in Marine Science*, 8, 643608. <https://doi.org/10.3389/fmars.2021.643608>
- Tian, H., Yang, Q., Najjar, R. G., Ren, W., Friedrichs, M. A. M., Hopkinson, C. S., & Pan, S. (2015). Anthropogenic and climatic influences on carbon fluxes from eastern North America to the Atlantic ocean: A process-based modeling study. *Journal of Geophysical Research: Biogeosciences*, 120(4), 752–772. <https://doi.org/10.1002/2014jg002760>
- Wang, G., Su, J., Ding, Y., & Chen, D. (2007). Tropical cyclone Genesis over the South China Sea. *Journal of Marine Systems*, 68(3–4), 318–326. <https://doi.org/10.1016/j.jmarsys.2006.12.002>
- Warner, J. C., Armstrong, B., He, R., & Zambon, J. B. (2010). Development of a coupled ocean-atmosphere-wave-sediment transport (COAWST) modeling system. *Ocean Modelling*, 35(3), 230–244. <https://doi.org/10.1016/j.ocemod.2010.07.010>
- Warner, J. C., Sherwood, C. R., Signell, R. P., Harris, C. K., & Arango, H. G. (2008). Development of a three-dimensional, regional, coupled wave, current, and sediment-transport model. *Computers & Geosciences*, 34(10), 1284–1306. <https://doi.org/10.1016/j.cageo.2008.02.012>
- Webster, P. J., Holland, G. J., Curry, J. A., & Chang, H. R. (2005). Changes in tropical cyclone number, duration, and intensity in a warming environment. *Science*, 309(5742), 1844–1846. <https://doi.org/10.1126/science.1116448>
- Wu, L. G., Wang, B., & Geng, S. Q. (2005). Growing typhoon influence on East Asia. *Geophysical Research Letters*, 32(18), L18703. <https://doi.org/10.1029/2005gl022937>
- Yao, Y., Tian, H., Pan, S., Najjar, R. G., Friedrichs, M. A. M., Bian, Z., et al. (2021). Riverine carbon cycling over the past century in the mid-Atlantic region of the United States. *Journal of Geophysical Research: Biogeosciences*, 126(5), e2020JG005968. <https://doi.org/10.1029/2020jg005968>

- Ye, H. J., Sui, Y., Tang, D. L., & Afanasyev, Y. D. (2013). A subsurface chlorophyll a bloom induced by typhoon in the South China Sea. *Journal of Marine Systems*, 128, 138–145. <https://doi.org/10.1016/j.jmarsys.2013.04.010>
- Ye, H. J., Yang, C., Tang, S., & Chen, C. (2020). The phytoplankton variability in the Pearl River estuary based on VIIRS imagery. *Continental Shelf Research*, 207, 104228. <https://doi.org/10.1016/j.csr.2020.104228>
- Yin, K. D., Song, X. X., Sun, J., & Wu, M. C. S. (2004). Potential P limitation leads to excess N in the Pearl River Estuary coastal plume. *Continental Shelf Research*, 24(16), 1895–1907. <https://doi.org/10.1016/j.csr.2004.06.014>
- Yu, L., Fennel, K., Laurent, A., Murrell, M. C., & Lehrter, J. C. (2015). Numerical analysis of the primary processes controlling oxygen dynamics on the Louisiana shelf. *Biogeosciences*, 12(7), 2063–2076. <https://doi.org/10.5194/bg-12-2063-2015>
- Yu, L., & Gan, J. (2022). Reversing impact of phytoplankton phosphorus limitation on coastal hypoxia due to interacting changes in surface production and shoreward bottom oxygen influx. *Water Research*, 212, 118094. <https://doi.org/10.1016/j.watres.2022.118094>
- Zhang, W. G., Wilkin, J. L., & Schofield, O. M. E. (2010). Simulation of water age and residence time in New York Bight. *Journal of Physical Oceanography*, 40(5), 965–982. <https://doi.org/10.1175/2009jpo4249.1>
- Zhang, Z., Wang, Y., Zhang, W., & Xu, J. (2019). Coastal ocean response and its feedback to Typhoon Hato (2017) over the South China Sea: A numerical study. *Journal of Geophysical Research: Atmospheres*, 124(24), 13731–13749. <https://doi.org/10.1029/2019jd031377>
- Zhao, H., Pan, J., Han, G., Devlin, A. T., Zhang, S., & Hou, Y. (2017). Effect of a fast-moving tropical storm Washi on phytoplankton in the northwestern South China Sea. *Journal of Geophysical Research: Oceans*, 122(4), 3404–3416. <https://doi.org/10.1002/2016jc012286>
- Zhao, H., Tang, D., & Wang, D. (2009). Phytoplankton blooms near the Pearl River Estuary induced by Typhoon Nuri. *Journal of Geophysical Research*, 114(C12), C12027. <https://doi.org/10.1029/2009jc005384>
- Zhao, Y., Uthairan, K., Lu, Z., Li, Y., Liu, J., Liu, H., et al. (2021). Destruction and reinstatement of coastal hypoxia in the South China Sea off the Pearl River estuary. *Biogeosciences*, 18(8), 2755–2775. <https://doi.org/10.5194/bg-18-2755-2021>
- Zheng, G. M., & Tang, D. (2007). Offshore and nearshore chlorophyll increases induced by typhoon winds and subsequent terrestrial rainwater runoff. *Marine Ecology Progress Series*, 333, 61–74. <https://doi.org/10.3354/meps333061>